Land subsidence and rebound in the Taiyuan basin, northern China, in the context of inter-basin water transfer and groundwater management

Wei Tang[1], Xiangjun Zhao[1], Mahdi Motagh[2,3], Gang Bi[4], Jing Li[1], Mingjie Chen[1], Hua Chen[5], Mingsheng Liao[6]

[1]College of Geoscience and Surveying Engineering, China University of Mining and Technology, Beijing, China (weitang@cumtb.edu.cn)

[2]GFZ German Research Centre for Geosciences, Department of Geodesy, Section of Remote Sensing and Geoinformatics, Potsdam, Germany

[3]Institute of Photogrammetry and GeoInformation, Leibniz University Hannover, Hannover, Germany

[4]Shanxi Institute of Surveying, Mapping and Geoinformation, Taiyuan, China

[5]School of Geodesy and Geomatics, Wuhan University, Wuhan, China

[6]State Key Laboratory of Information Engineering in Surveying, Mapping and Remote Sensing, Wuhan University, Wuhan, China

Abstract

The freshwater scarcity and sustainability of overexploited aquifers have been recognized as a big threat to global water security for human development. Consequently, much research has focused in the past on negative consequences of groundwater abstraction, but somewhat less has been documented about the impacts of adequate management practices to address water shortages. Here, using an integrated analysis of InSAR displacement data, groundwater, and geophysical modeling we show how combined management provisions and inter-basin water transfer project has affected the aquifer system in Taiyuan basin in North China. Following groundwater recovery, the alleviation of land subsidence was found with rates being reduced by up to ~70% in the period 2017-2020 with respect to the period 2007-2010. The increase in pore pressure caused by rising groundwater in Taiyuan city, north of the basin, turned

four subsidence centers with rates exceeding 110 mm/yr in the 1980 to uplift centers with rates up to +25 mm/yr between 2017-2020. A simple linear elastic model for homogenous subsurface properties can explain InSAR-measured surface displacements well. In the central basin, we found a significant seasonal displacement with annual amplitude up to 43 mm (negative peak in autumn and positive peak in spring) related to the groundwater recharge and discharge due to agricultural pumping irrigation. Using cross-wavelet method, we showed a relatively short time lags (less than one month) between surface deformation and water level changes in the central basin, indicating the low-permeability clayey units have a limited influence in delaying the compaction of aquifer system. Quantifying the effects of adequate groundwater management measures and large-scale engineering approaches like inter-basin water transfer to recharge pumped aquifers provide insight for local governments and decision-makers to properly evaluate the impacts of their policy in recovering the sustainability and efficiency of aquifers in water-deficient basins.

1. Introduction

Growing populations, increasing urbanization and intensive agriculture have led to excessive exploitation of groundwater resources, particularly in dry regions where surface water availability is limited (Chen et al., 2016; Famiglietti and Ferguson, 2021; Jasechko and Perrone, 2021; Motagh et al., 2008). Changing climate conditions have been increasing reliance on water resources through altering precipitation patterns, more drought occurrence, and increasing temperatures and evapotranspiration (Herrera-García et al., 2021; Shao et al., 2017). Areas of groundwater depletion typically occur in irrigated agricultural regions crucial to food security, such as the Northwestern India (Long et al., 2016), the U.S. High Plains (Scanlon et al., 2012), Iran central Plateau (Haghshenas Haghighi and Motagh, 2019; Motagh et al., 2017), and the North China Plain (NCP) (Feng et al., 2013; Gong et al., 2018). The severity of the problem in Taiyuan basin of Shanxi Province (Fig. 1), bordering the NCP, is among the

highest, due to its arid condition (annual rainfall < 400 mm) and critical water scarcity (water resource per capita < 400 m^3). Adding to the problem is the fact that large-scale coal mining in this province is a water-intensive process, which is accounting for 20% in total water use (Qiao et al., 2011; Shanxi Provincial Bureau of Statistics, 2019). At the same time, the mining activities pollute surface water, reducing the availability of clean water and increasing groundwater exploitation. The annual amount of exploited groundwater in Taiyuan basin, the most important industrial and agricultural base in Shanxi Province, was ~10.82 million m^3 in 1970, and this figure rose up to 450.78 million m^3 in 2000 (Fig. 1c), accounting for about 65% of the total water supply. The intense groundwater exploitation has caused depletion of rivers and aquifers at an alarming rate and as a consequence the ecological environment has been severely degraded.

Land subsidence is one of the environmental consequences of overuse of groundwater in the basin, which is often overlooked or underrated because of its slowly developing characteristic. The groundwater-related subsidence was first discovered in 1956 in the north of the basin in Taiyuan city (Ma et al., 2006) where the maximum cumulative subsidence had exceeded 3.1 m by 2007 and the affected area was over 552.9 km^2 (Yang, 2015). Land subsidence may last for a long time (several decades or more). The growing availability of Synthetic Aperture Radar (SAR) images acquired from different radar satellites, allows to monitor the spatial and temporal evolution of ground subsidence processes in a longer time scale (Haghshenas Haghighi and Motagh, 2019; Riel et al., 2018; Zhao et al., 2019). Using different sets of SAR data imaging at different look angles also allows to investigate the three-dimensional (3-D) ground deformation (Fuhrmann and Garthwaite, 2019; Pepe and Calò, 2017). Liu et al. (2018) studied the long-term subsidence between 1992 and 2015 in a portion of Taiyuan basin (around Taiyuan city) using Interferometric SAR (InSAR) technique and multi-sensor SAR images. They revealed a maximum subsidence rate of 80 mm/yr occurring in the southern suburb of Taiyuan city during the period of 2009-2015. They also observed

land uplift in northern Taiyuan city with a rate around 10 mm/yr from 2004 to 2005. Land uplift could be resulted from the expansion of the granular skeleton due to the increasing pore pressure associated with groundwater recovery, a phenomenon referred to as elastic or poroelastic rebound (Waltham, 2002). Such measurements of surface movement from InSAR can reflect changes in groundwater level and geological conditions deep below the earth's surface, which have been used to predict groundwater flow in old coalfields (Gee et al., 2020). Seasonal land subsidence and uplift can occur from seasonal groundwater declines and recoveries related to seasonal groundwater withdrawal and recharge from artificial and natural events (Hoffmann et al., 2001). These seasonal subsidence and rebound were detected from InSAR at a high spatial detail which were further used to estimate the elastic storage coefficient for aquifer systems and characterize fault properties (Chaussard et al., 2016; Hoffmann et al., 2001; Riel et al., 2018). These previous studies also demonstrate the benefits of InSAR technique for groundwater management to maintain sustainable pumping practices.
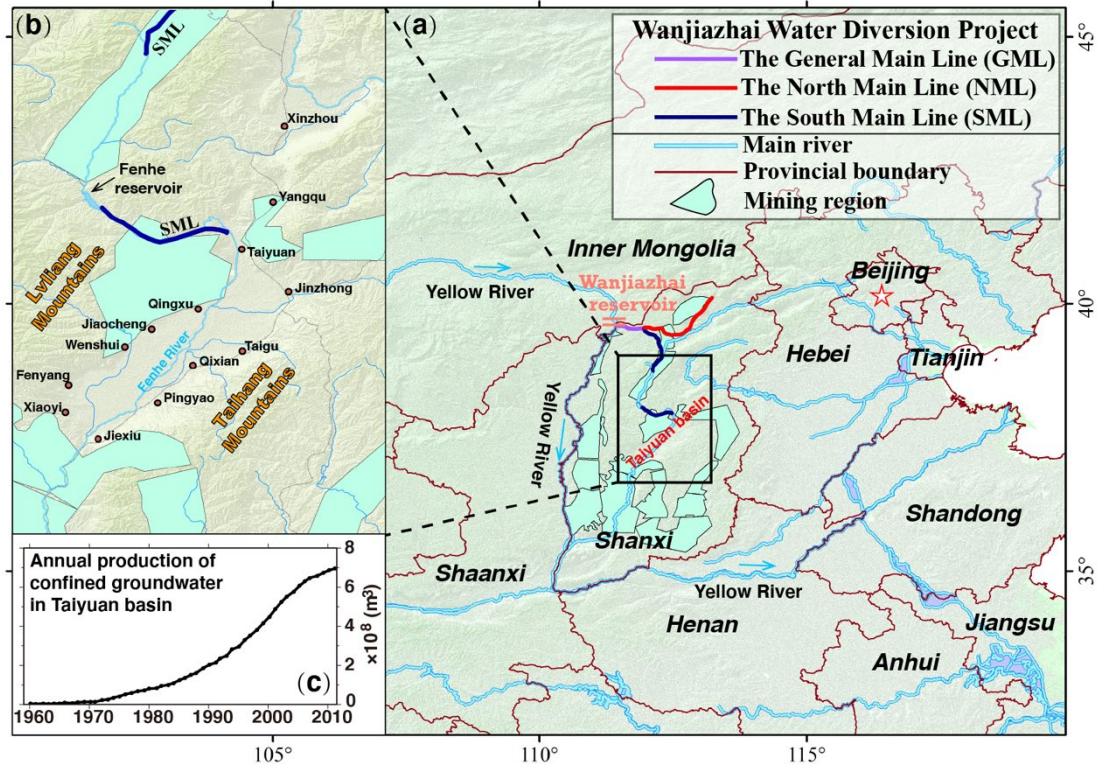

Fig.1. (a) Location of the Taiyuan basin. The three routes of the Wanjiazhai Water Diversion project are shown in the map. (b) Close-up view of our study area. The red

101   points show the main cities in the basin. Mining regions around the basin are shown in

102   the figure. (c) History of groundwater production in Taiyuan basin (Sun et al., 2016).

103   Inter-basin water transfer schemes, i.e., transfer water from areas with perceived

104   surpluses to those with shortages, are widely considered as the quick fix solution to

105   addressing water pressures in water poor areas. The Wanjiazhai Water Diversion

106   (WWD) project was designed to transport water from Yellow River to solve this

107   problem in Shanxi Province (Fig. 1). With a total length of 441.8 kilometers, this project

108   aimed to divert 1.2 billion m^3 of water each year from Yellow River, in which 640

109   million m^3 to Taiyuan city through the South Main Line (SML) and 560 million m^3 to

110   Datong and Shuozhou through the North Main Line (NML) (Xie et al., 1999). Since its

111   operation in 2003, a total of 2.87 billion m^3 of water has been transferred to Shanxi

112   Province by the end of 2018. Of this, 1.73 billion m^3 has been used for household and

113   1.14 billion m^3 for the purpose of ecological restoration.

114   Transfer project may not necessarily meet water needs in such an arid region with

115   a rapidly growing economy, and therefore better local management of resources is

116   needed to keep pace with escalating water demands. Since 2007, the provincial

117   government has implemented an integrated, inter-municipal, and multi-objective

118   program to restoring ecosystem in the basin (Falke, 2016): water conservation policies

119   and closing wells curtail extensive water use; a large-scale afforestation program

120   increases water retention and reduces soil erosion, whilst the modernization of

121   irrigation system improves the efficiency of water use. In these cases, the amount of

122   groundwater exploitation significantly reduced and a gradual rise of water level

123   occurred.

124   Although the WWD project and local management practices have implemented

125   for over one decade, their efficiency in recovering the overexploited aquifer system

126   across the whole basin has not been evaluated. Accurate maps of surface subsidence

127   and uplift related to groundwater drawdown and rebound from InSAR with high spatial

128   and temporal resolution allow us to have a better understanding on how and where

129   aquifer recovers (Teatini et al., 2011; Thangarajan and Vijay P., 2016).

130   Here, we present promising effects of this transfer project together with

131   complementary management practices caused to Taiyuan basin from the perspective of

132   ground displacement maps obtained by the analysis of a full archive of SAR data from

133   ENVISAT (2007-2010), ALOS-1 (2007-2011) and Sentinel-1 (2017-2020). We first

134   applied Small Baseline Subset (SBAS) time series analysis (Berardino et al., 2002;

135   Hooper, 2008; Tong and Schmidt, 2016) to extract ground displacement maps from the

136   full archive of SAR images in Taiyuan basin. We addressed the issue of tropospheric

137   delay and its impact on the seasonal deformation by combing GACOS (Generic

138   Atmospheric Correction Online Service) (Yu et al., 2018b) and a common point

139   stacking method (Tymofyeyeva and Fialko, 2015). The accuracy of InSAR

140   displacements was validated with ground truth data from seven continuous GPS in the

141   basin. We reconstructed spatially continuous maps of seasonal amplitude and phase

142   within the basin to study the effects of groundwater pumping for agriculture and

143   irrigation on the ground response. We further analyzed the time-lag effects between

144   displacement and groundwater levels by a cross-wavelet method to quantify their causal

145   relationships. By an integrated use of groundwater level maps and InSAR displacement

146   data, the spatiotemporal evolution of natural ground displacement following the

147   groundwater recovery has been analyzed. The results of our study promote a better

148   understanding of spatiotemporal patterns of aquifer recovery at a basin scale in Taiyuan,

149   which can aid to optimize the allocation scheme of imported water resources under the

150   background of water transfer project.

2. Description of study area

2.1 Geologic settings

Taiyuan basin is a large-scale Cenozoic rift basin which is tectonically bounded by the Taihang Mountains to the east and the Lvliang Mountains to the west (Fig. 2a). The altitude is high in the northwest (~1500 m) and decreases towards the southeast in the basin (~730 m to ~790 m), with an average elevation of 800-900 meters in the central basin. Such terrain features are resulted from the neotectonic movements (Tang et al., 2013). Areas in the central basin are broad and flat alluvial plain, characterizing by dense population and fertile soil, which is the highest agricultural production zone in Shanxi Province.
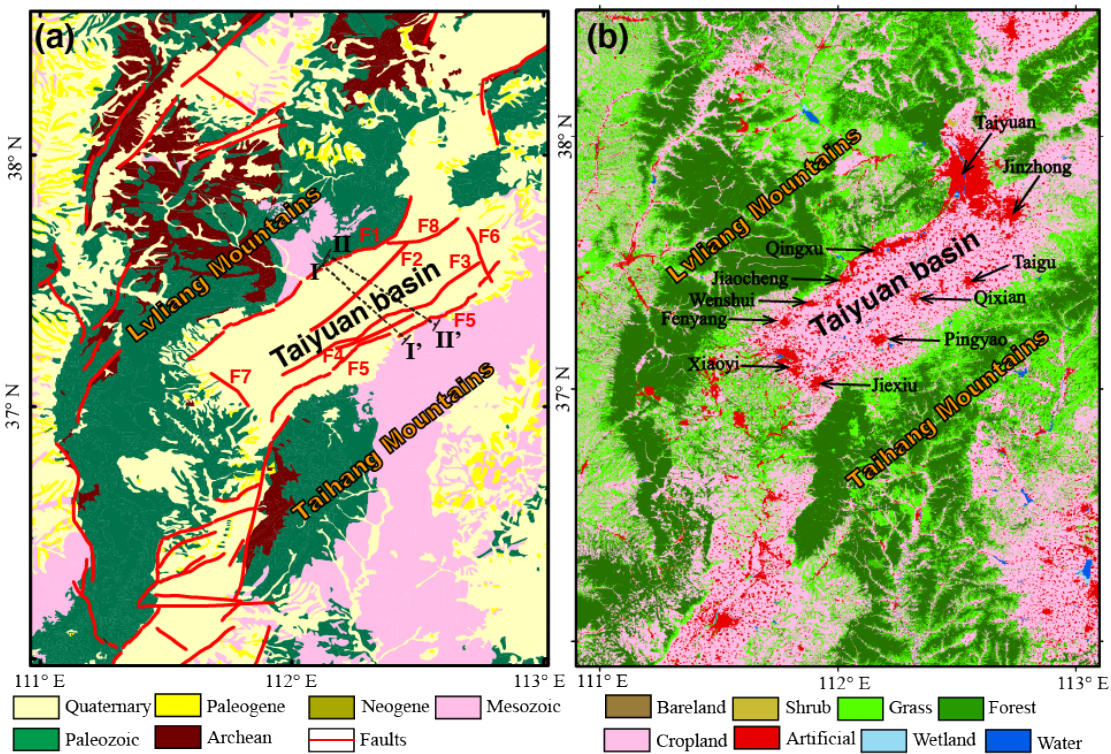

Fig. 2. (a) Geological map of the Taiyuan basin. Geological cross-section lines I-I' and II-II'. F1, Jiaocheng fault; F2, Longjiaying fault; F3, Qixian fault; F4, Pingyao–Taigu fault; F5, Hongshan–Fancun fault; F6, Yuci–Beitian fault; F7, Sanquan fault; F8, Tianzhuang fault. (b) The 30-meter resolution land cover in the study area, obtained from GlobeLand30 (Chen et al., 2014). The arrows indicate the main cities in the basin.

167   The geological structure is mainly controlled by the joint effect of Jiaocheng

168   Depression in the late Cenozoic fault zone of Shanxi platform and the fault terraces in

169   the west of the basin (Tang et al., 2013). The main active faults around the basin are

170   (Fig. 2a): Jiaocheng fault (F1), Hongshan–Fancun fault (F5), Yuci–Beitian fault (F6),

171   Sanquan fault (F7), and Tianzhuang fault (F8). The Jiaocheng fault (F1), located in the

172   western edge of the basin, is a high-angle normal fault extending from the north on the

173   mountains in the west of Taiyuan city to the south in Fenyang, with a length of ~130

174   km and an SE dip (Xie et al., 2008). The eastern basin is bounded by the Hongshan–

175   Fancun fault (F5), which is also a high-angle normal fault with an NE (45°) trend, an

176   NW dip, and a length of ~100 km (Xie et al., 2004). Yuci–Beitian fault is a boundary

177   fault on the northeastern boundary of Jinzhong basin, extending in the NNW-SSE

178   direction with an SWW dip, with a length of ~34 km (Chen et al., 2003). Sanquan fault,

179   in the southwestern boundary of the basin, has an NNW trend and an ENE dip. Except

180   for the active faults, hidden faults are developed, including Longjiaying fault (F2),

181   Qixian fault (F3), Pingyao–Taigu fault (F4), and Tianzhuang fault (F8). As can be seen

182   from the geological section I-I' in Fig.3a, the strata across the hidden faults are

183   significantly disrupted that the hanging wall is dropped, which caused a small

184   separation in the shallow layers and a large separation in the deeper layers. This

185   indicates that the hidden faults are synsedimentary faults or growth faults (Peng et al.,

186   2018). In the flat basin, the principal land cover are agricultural lands (Fig. 2b),

187   covering approximately 70% of the territory, and artificial surface, extending over most

188   of the rest (29.5%). Water bodies make up less than 1% of the total land cover.

189   **2.2 Hydrological conditions**

190   Groundwater in Taiyuan basin gets recharged mainly through the lateral flow of

191   water from the surrounding areas. Some of the recharge comes from the infiltration of

192   surface water from Fenhe River (Qiao et al., 2011), which is the main river in the basin,

193   originating from the northwestern mountain and running through the basin from north

to south (see Fig.1). Cenozoic sediments with a thickness between 50 and 3,800 m occur all over the basin, and the types of sediments within the vadose zone mainly include clay, silty clay, loam sand, silty sand, and fine sand (Guo et al., 2007). The basin's aquifer system can be divided into four group (Fig.3b): (1) Quaternary Holocene unconfined aquifer (depth<50 m in depth), (2) Quaternary Late and Middle Pleistocene confined aquifer (depth from 50 m to 200 m), (3) Quaternary Early Pleistocene lacustrine–alluvial weak aquifer (depth from 200 m to 400 m) and (4) Neogene red soil with thin layers of sandy gravel lacustrine weak confined aquifer (Peng et al., 2018).
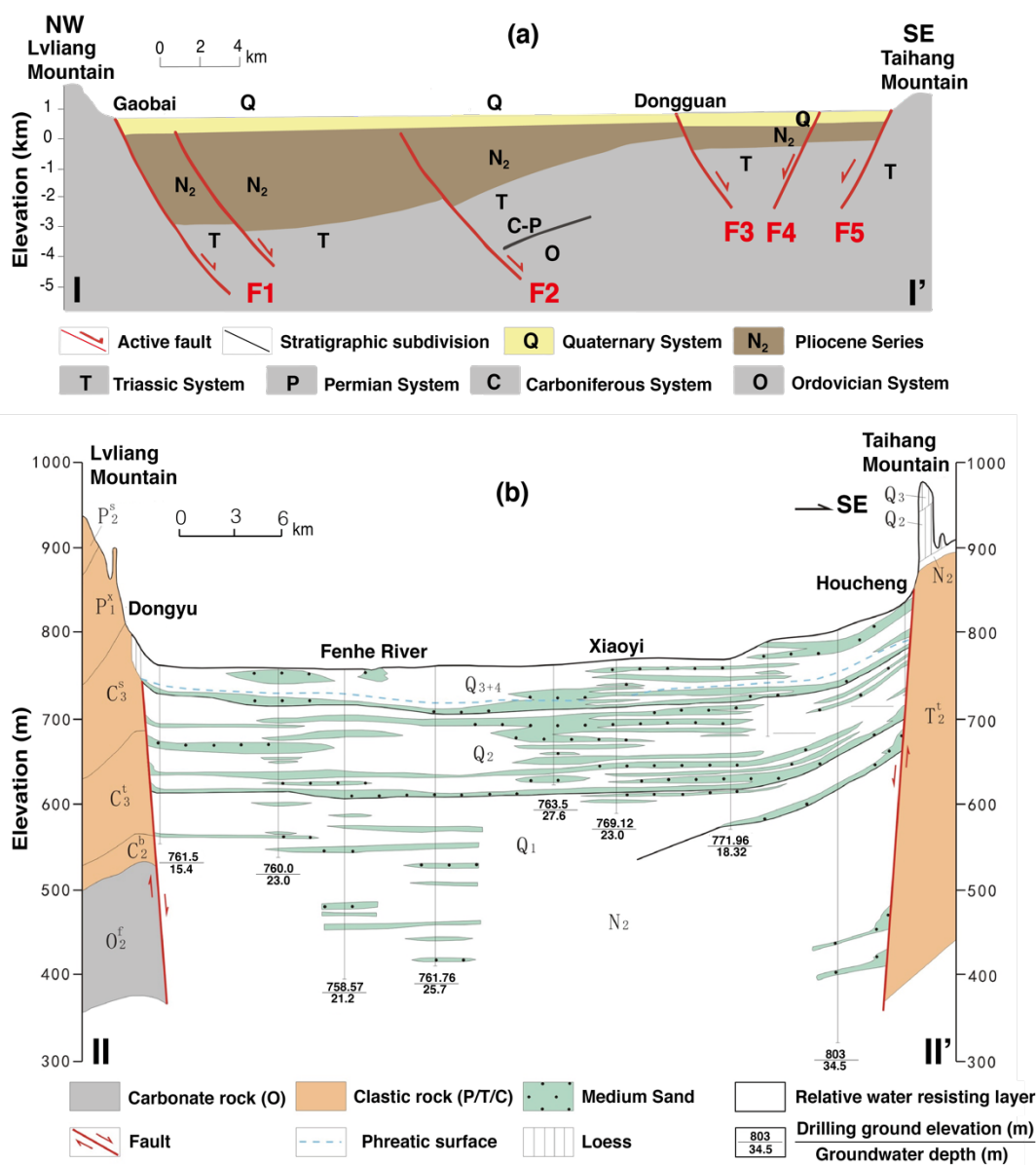
204   Fig.3. (a) Geological profile (I-I') and (b) hydrogeological profile (II-II') in the Taiyuan

205   basin, adapted from (Peng et al., 2018). The profile locations were found in Fig.2.

206   Shallow unconfined aquifers, ranging from 10 to 30 m, are distributed throughout

207   the basin (Peng et al., 2018). The lithology of shallow unconfined aquifer is mainly

208   alluvial and diluvial sand and gravel of Holocene and Late Pleistocene. The lithology

209   in the middle and deep confined aquifers is alluvial and lacustrine sandy pebbles of

210   Early, Middle and Late Pleistocene, with fine, medium, and coarse sand presented. The

211   aquiclude is mainly composed of silty clay, which forms the multi-layered confined

212   aquifers with a depth of 50–200 m and a thickness of 5–50 m (Han et al., 2008). Deep

213   groundwater (depth > 200 m) mostly occurs in the southern part of the basin near the

214   city of Fenyang and Wenshui.

215   **3. Datasets and preprocessing**

216   **3.1 InSAR datasets and interferograms generation**

217   Seven SAR datasets acquired from three radar sensors (Table 1), including

218   ENVISAT, ALOS-1 and Sentinel-1 satellites, were selected in our study. Data from

219   ENVISAT and ALOS-1 between 2007-2010, and data from Sentinel-1 between 2017-

220   2020, enable us to investigate temporal changes of ground deformation before and after

221   the operation of the WWD project. The SAR images regularly acquired with 12-days

222   repeating period from Sentinel-1 are an excellent data source for analyzing seasonal

223   deformation and quantifying the aquifer parameters in the basin.

224   We used GMTSAR (Xu et al., 2017) to process ALOS-1 and Sentinel-1 images

225   and DORIS (Delft object-oriented radar interferometric software) (Kampes and Usai,

226   1999) to process ENVISAT images to generate interferograms. Topographical phase

227   effects were removed using a digital elevation model (DEM) from the Shuttle Radar

228   Topography Mission (SRTM) with approximately 30 m spatial resolution (Farr et al.,

229   2007). The number of generated interferograms for each SAR dataset are listed in Table

1. The unwrapped solution for each interferogram were obtained with SNAPHU (Statistical-Cost, Network-Flow Algorithm for Phase Unwrapping) software (Chen and Zebker, 2001). After that, the ground displacements were retrieved by InSAR time series method as described in Section 4.1.

Table 1. SAR datasets used in our study. N_{SAR} is the number of SAR scenes and N_{int} is the number of interferograms. The time format is given in YYYYMMDD (Y=year, M=month, D=day).

Sensor	Track/orbit	Frame	Direction	Period	N_{SAR}	N_{int}
ENVISAT	75	78	Descending	20030817-20100919	39	79
ALOS-1	455	740	Ascending	20070115-20110313	20	39
ALOS-1	456	740	Ascending	20070201-20101228	15	32
ALOS-1	457	730	Ascending	20070103-20110301	20	39
Sentinel-1	113	116+121	Ascending	20170319-20200420	94	288

3.2 Continuous GPS observations

There are eight continuous GPS (CGPS) sites located within our study area (Table 2). The 3D (north-south, east-west, and up-down) velocities for each GPS stations in the ITRF 2008 reference frame are listed in Table S1. The K001 station is selected as the reference point because the observed displacements at this location are stable compared to other stations. The 3D linear velocities for each station with reference to K001 are listed in Table 2. The displacement time series are shown in Supplementary Material Fig. S1. The CGPS data are spanning the period from 2016 to 2019 with daily solutions, which is partly coincided with the time period of Sentinel-1 data. All stations except for A002 exhibit very small horizontal movements (~-4 to ~4 mm/yr) compared to the vertical component. We concluded that the ground deformation occurred mainly in the vertical direction, which is consistent with the fact that groundwater pumping principally induced vertical land subsidence. The CGPS measurements will be used to validate our InSAR displacement results in Section 5.1.

Table 2. Linear velocity data for CGPS in the local reference frame (used K001 site as
the reference point).

Station	Lon (°)	Lat (°)	Time period	North [mm/yr]	East [mm/yr]	Up [mm/yr]
A001	112.54	37.87	20160101-20190516	-0.61±0.16	-2.22±0.12	10.33±0.37
A002	112.35	37.60	20160101-20190619	-11.86±0.11	1.93±0.07	-11.85±0.22
A008	112.53	37.87	20160101-20181118	-1.10±0.11	-3.68±0.09	12.00±0.24
J004	111.78	37.24	20160101-20190516	0.06±0.23	-2.12±0.16	-0.41±0.44
J005	112.15	37.53	20160101-20190516	0.72±0.21	4.44±0.15	-12.46±0.38
K002	112.35	37.35	20160104-20190516	-1.35±0.17	-2.17±0.11	-2.66±0.36
K003	111.91	37.04	20160101-20190516	-0.87±0.17	-1.26±0.12	-33.53±0.36

3.3 Groundwater level data

We have access to groundwater level data at four water wells acquired from China Earthquake Networks Center (CENC). All wells were drilled into consolidated rocks and water level in confined aquifers were recorded since 1970s or 1980s (Yan et al., 2020). The basic information of the four water wells is listed in Table 3. The depths of water wells range from 315 m to 765.78 m and the aquifer lithology differs at each well, as shown in Table 3. The water level data at these four wells are available from 2007 to 2020 which coincide with periods for both ENVISAT and Sentinel-1 data. In addition, we acquired another two well data (TG and PY) from published literature (Sun et al., 2016) which are available from 2003 to 2010 that overlap with the time period of ENVISAT data. We will investigate the ground surface response to long-term changes as well as seasonal variations of groundwater at these water wells. In addition, several groundwater level contour maps collected from literatures (Han et al., 2008; Ma et al., 2006, 2005) and from local water management departments are used to evaluate the coupled effects of groundwater rebound and land uplift in Taiyuan city in the north of the basin.

Table 3. Information of the well stations. The information at TY, QXC, XY and JX are referred to (Yan et al., 2020).

Well name	Lon (°)	Lat (°)	Depth (m)	Aquifer lithology
TY	112.43	37.71	765.78	Limestone & dolomite

QXC	112.23	37.37	442.19	Metamorphic volcaniclastic rock
XY	111.77	37.15	502.93	Fine sandstone intercalated with shale
JX	111.90	37.02	315	Loess and sandy clay
TG	112.53	37.43	-	-
PY	112.28	37.20	-	-

4.Methods

4.1 GACOS-assisted small baseline InSAR method

Tropospheric effect is one of the main challenges in InSAR application. It can be spatially divided into two components: stratified delay and turbulent delay. The stratified component is spatially correlated with topography and exhibits temporally systematic (e.g., seasonal) variations, whereas the turbulent component is expected to be uncorrelated both in space and time. Many approaches have been proposed to mitigate the tropospheric delays either from phase data itself by spatial-temporal filtering or from external data (e.g., GNSS, MERIS/MODIS, global atmospheric models (GAMs), etc.). Spatial-temporal filtering methods are based on the assumption that tropospheric delay is randomly distributed in time. Such assumption may not hold, because a systematic, temporally correlated component of delay exists due to the repeatable seasonal cycle of atmospheric states, which are usually dominated by the stratified component (Fattahi and Amelung, 2015). Thus, the temporally correlated part of the delays cannot be properly filtered out, producing a bias in the results. The approaches relying on GAMs tend to become a common practice in InSAR community due to the global data availability. GACOS is one of such approaches which incorporates weather data into an Iterative Tropospheric Decomposition (ITD) model to provide high spatial resolution, globally available and near real time delay product (Yu et al., 2018a). This method has been validated its effectiveness in mitigating the

291 long-wavelength and topography-dependent atmospheric noises in InSAR
292 interferograms.

293   In our study area, the topography surrounding the basin varies from ~1km in
294 eastern Taihang Mountains to ~3 km in western Lvliang Mountains. Such significant
295 terrain variations are expected to produce strong atmospheric delays across the
296 mountainous region. Indeed, many interferograms show a strong correlation between
297 phase and elevation, as shown in Fig. 4. The phase-elevation dependency can be
298 visually observed by comparing the topography map and the unwrapped interferograms
299 and quantitatively evaluated by the correlation coefficient (indicated as R in Fig. 4). It
300 can be seen that the interferogram 20180125-20180206 is dominated by a strong
301 elevation-related delays and the correlation coefficient is as high as -0.79. After
302 GACOS correction, the phase-elevation dependence was significantly reduced, with
303 the fitted linear function (red line) approaching vertical line and the correlation
304 coefficient reduced to -0.17. The interferogram 20180910-20180922 is also dominated
305 by stratified delay and GACOS can reasonably mimic the interferogram. Although the
306 phase-elevation dependence reduced after correction, the correlation coefficient
307 changed from a negative value of -0.70 to a positive value of 0.39. It implies that
308 GACOS tends to overestimate the stratified delays, which can be observed in the
309 corrected interferogram in Fig. 4 (see the red ellipse). For interferogram 20181028-
310 20181109, however, which is dominated by turbulent delays, GACOS is failed to
311 reproduce the small-scale, wave-like spatial patterns associated with mountain lee
312 waves (Kinoshita et al., 2017). The correlation coefficient is only -0.07 in the
313 uncorrected interferogram and it increases to 0.33 after correction, indicating that
314 GACOS incorrectly introduced a phase-elevation dependence into the result. It further
315 implies that in the case of a dominant turbulent delay in the interferograms, the GACOS
316 delay products tend to overestimate the phase-elevation dependence.

317   From the above example, we infer that the GACOS method suffers from the
318 following problems: (i) it cannot fully capture the small-scale turbulent effects in the

319 interferograms due to the limited resolution of the weather model data (currently 0.1

320 degree spatially and 6 hours temporally), (ii) the ITD model may overestimate the

321 phase-elevation dependency under the circumstance of a strong turbulent atmosphere.

322 These limitations need the user to be careful when implementing the GACOS correction

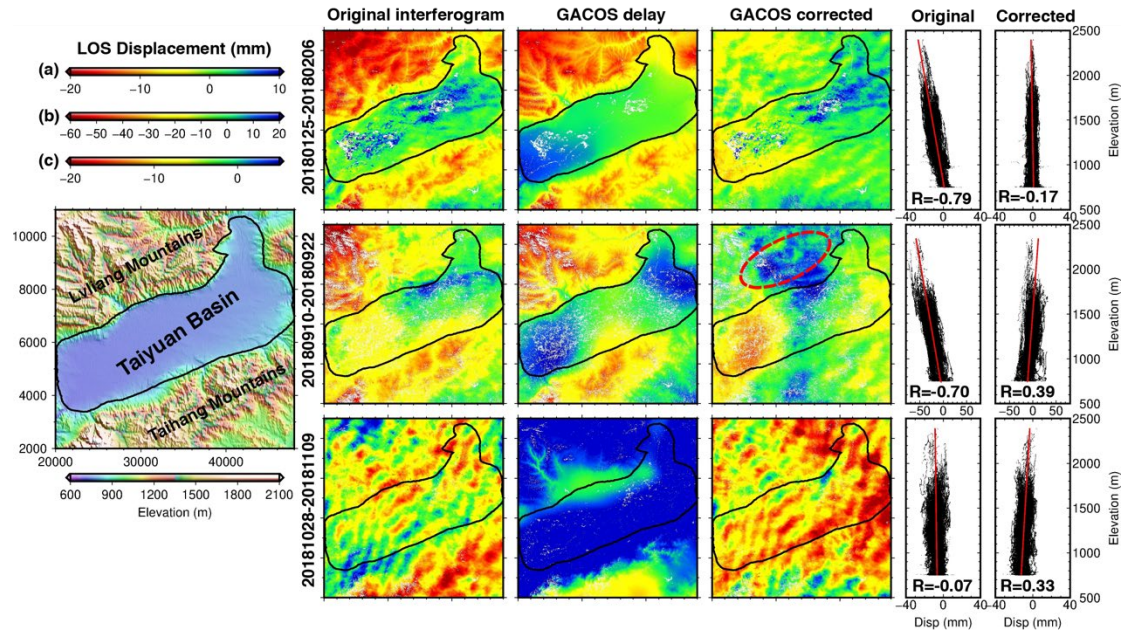323 for both conventional D-InSAR and time series InSAR applications (Shamshiri et al.,

324 2020).

325

326 Fig. 4. The atmospheric effects and corrections by GACOS on independent

327 interferograms from Sentinel-1 dataset collected at different times. Note the differences

328 in color scale: (a) is applied to interferogram 20180125-20180206, (b) is applied to

329 interferogram 20180910-20180922 and (c) is for interferogram 20181028-20181109.

330 The interferograms are in radar coordinate.

331   In this study, we developed a more reliable method to mitigate tropospheric effects

332 in time series analysis. We first corrected the stratified component for each

333 interferogram using atmospheric products from GACOS. Since the temporal-correlated

334 part (seasonal variations) of stratified delays have been removed by GACOS, the

335 remaining delay tend to better meet the basic assumption of temporally uncorrelated

336 noises in the time series analysis. As a result, the accuracy of the estimate of the

337 remaining delay can be improved by averaging of redundant interferograms that share

338 a common acquisition.

339   After removing the flat-earth and topographic contributions, the phase in

340 unwrapped interferogram can be expressed as:

341
$$\Delta\emptyset_{int} = \Delta\emptyset_{disp} + \Delta\emptyset_{stra} + \Delta\emptyset_{turb} + \Delta\emptyset_n \tag{1}$$

342 where $\Delta\emptyset_{disp}$ is the ground displacement, $\Delta\emptyset_{stra}$ and $\Delta\emptyset_{turb}$ are the stratified and

343 turbulent delay, respectively. $\Delta\emptyset_n$ represents the other errors (the residual orbital error,

344 the DEM error, and the antenna noise). After corrected the stratified delay by GAOCS,

345 the phase can be expressed as:

346
$$\Delta\emptyset_{int-stra} = \Delta\emptyset_{disp} + \Delta\emptyset_{turb} + \delta_{stra} + \Delta\emptyset_n \tag{2}$$

347 where δ_{stra} is the residual after GACOS correction. Since most parts of stratified

348 delays have been subtracted, the residual δ_{stra} is a short-scale and random noise,

349 which is mainly correlated with the turbulent delays, and the two terms $\Delta\emptyset_{turb}$ and

350 δ_{stra} are combined into one as $\Delta\emptyset_{turb}$. Thus, the residual phase in Equation (2) in two

351 interferograms with acquisition dates t_1, t_2 (common date), and t_3, can be expressed

352 as:

353
$$\begin{cases} \Delta\emptyset_{int-stra}^{1,2} = \Delta\emptyset_{disp}^{1,2} + \emptyset_{turb}^2 - \emptyset_{turb}^1 + \Delta\emptyset_n^{1,2} \\ \Delta\emptyset_{int-stra}^{2,3} = \Delta\emptyset_{disp}^{2,3} + \emptyset_{turb}^3 - \emptyset_{turb}^2 + \Delta\emptyset_n^{2,3} \end{cases} \tag{3}$$

354   The term $\emptyset_{turb}^2$ on the common date t_2 can be estimated by differencing the

355 two interferograms, $\Delta\emptyset_{int}^{1,2} - \Delta\emptyset_{int}^{2,3}$, assuming the two interferograms have the same

356 time span and ground displacement occurs at a steady rate., as follows:

357
$$\emptyset_{turb}^i = \lim_{N\to\infty} \frac{1}{2N} \sum_{j=1}^N [\Delta\emptyset_{int-stra}^{i,i-j} - \Delta\emptyset_{int-stra}^{i+j,i}] \tag{4}$$

358 where N is the number of SAR acquisitions. We called this algorithm as Common

359 Point Stacking method (hereafter called CPS method).

360   The CPS method would be exact if the deformation signal is linear or quasi-linear

361 over the time and a sufficiently large number of SAR scenes is available and acquired

362 with regular interval. This is not always the case such as in our study area, where there

363 exists seasonal variations of deformation associated with groundwater discharge and

recharge. We therefore used an iterative procedure to improve the estimates of atmospheric delays (Tymofyeyeva and Fialko, 2015; Wang and Fialko, 2017). We first estimated the rough LOS displacement applying a relatively strong smoothing in temporal dimension. The rough estimates of displacement were subtracted from the GACOS-corrected interferograms to update the atmospheric noise. In the next iteration, the updated atmospheric maps were removed from the interferograms, and a reduced temporal smoothing was adopted to re-estimate the LOS displacement time series. We reduced the amount of smoothing gradually in each iteration step to allow for recovering the non-linear displacement. This process repeated until convergence criteria were met. Finally, we subtracted the obtained turbulent delay maps from the GACOS-corrected interferograms and constructed the LOS displacement time series from the atmosphere-corrected phases by the coherence-based SBAS method (Tong and Schmidt, 2016). This coherence-based SBAS method is based upon the method of (Berardino et al., 2002), with a modification by incorporating phase coherence into the displacement inversion to suppress noises from decorrelated pixels.

4.2 Seasonal displacement and cause-effect mechanism analysis

We expect two different mechanisms to the ground deformation in the basin. First, the long-term decline of groundwater causes the compaction of fine-grained soil, which leads to the long-term and mainly inelastic land subsidence. Second, a seasonal elastic deformation superimposed on the longer-term trend, which is caused by charging and discharging of groundwater in the aquifer system in winter and summer. Thus, we model the time series as a summation of sine and cosine functions with annual and semiannual periodicities for the seasonal cycle and a linear fit for the long-term trend as:

$$d(t) = b + v \cdot t + \sum_{k=1}^{2} S_k \sin(2\pi kt) + C_k \cos(2\pi kt) + \varepsilon \qquad (5)$$

where v is the linear velocity and b is the intercept; S_k, C_k are the coefficients of the annual terms ($k = 1$) and of the semiannual terms ($k = 2$), respectively. The last

391 term ε represents noise. We estimate the coefficients b, v, S_k and C_k using least

392 squares regression. Then, the annual and semiannual amplitudes A_k and phase delays

393 $\emptyset_k$ (or time to peak signal) can be computed as:

$$A_k = \sqrt{S_k^2 + C_k^2}, \ \ \emptyset_k = \tan^{-1}\frac{S_k}{C_k}, \ \ k = 1,2 \tag{6}$$

394

395 To further understand the existing relationship between ground displacement and

396 the principal driving factor—groundwater level change, we quantitatively analyze the

397 correlations between the time series of surface displacement and groundwater level.

398 This is conducted by the Cross Wavelet Transform (XWT) method, which permits to

399 identify the common cross-wavelet power and the phase shift between the two time

400 series in the time-frequency domain (Grinsted et al., 2004; Tomaoós et al., 2020). The

401 XWT is computed by multiplying the Continuous Wavelet Transform (CWT) of a time

402 series by the complex conjugate of the CWT of the second time series. The phase shift

403 ($\Delta\emptyset$) of XWT represents the time delay or time lag (Δt) between the two time-series

404 that can be calculated as:

$$\Delta t = \frac{\Delta\emptyset * T}{2\pi} \tag{7}$$

405

406 where T is the periodicity or wave period of interest. Therefore, by applying XWT, it

407 is possible to find the correlations and the time-lag effects between seasonal variations

408 in the surface displacements and groundwater level changes.

409 **4.3 Modelling land uplift**

410 If we consider a shrinking reservoir within a linear pore elasticity medium, we can

411 determine the impact of volumetric strain on a reservoir on the ground surface by

412 integrating the solution associated to a point deformation source, which is referred to

413 as a nucleus of strain (Geertsma, 1973). Assume the reservoir is a flattened cylinder of

414 radius R, thickness h, depth D, and which thickness variation (compaction or

415 expansion) due to pressure change is given by Δh. The elastic earth is treated as a

416 homogeneous, isotropic and elastic half-space with Poisson's ratio v. The surface

displacement in the vertical component at a radial distance r (distance from reservoir center axis) can be expressed as follows:

$$u(r) = 2(v-1)\Delta h R \int_0^\infty e^{-D\alpha} J_1(\alpha R) J_0(\alpha r) d\alpha \qquad (8)$$

where Δh is determined by the initial reservoir thickness h, the increase of pressure ΔP and the Young's modulus E as $\Delta h = h\Delta P/E$. J_1 and J_0 are the Bessel functions of zero and first order, α is the variable used for integral operator.

In Taiyuan city, the underlying structure can be described by clay interlayers with spatially varying thickness ranging from 50 m to 200 m (Ma et al., 2006; Tang et al., 2018). We applied the analytical model to the northern uplift region with a reservoir height of 50 m and a depth of 800 m, and to the southern uplift region with a reservoir height of 140 m and a depth of 750 m. The elastic Earth is treated as an elastic half-space with an average Poisson's ratio of $v = 0.3$ in the shallow subsurface. We choose a typical values of soil Young's modulus of 25 MPa according to the granular material and its cohesive property in this area (Han et al., 2008; Ma et al., 2006). The pressure changes (ΔP) in the reservoir due to groundwater level change (Δl) can be computed as $\Delta P = \rho g \Delta l$, where ρ is corresponding to water density (1000 kg/m^3), g is acceleration of gravity (9.81 m/s^2).

5.Results and analysis

5.1 Validation of InSAR results

To assess the effectiveness of the GACOS-assisted SBAS method, four different methods were compared: (i) the SBAS method without atmospheric correction (hereafter called SBAS without atm); (ii) the SBAS method only with GACOS corrections (hereafter called SBAS-GACOS); (iii) the SBAS method only applying CPS method (hereafter called SBAS-CPS); (iv) our proposed GACOS-assisted SBAS method (hereafter called SBAS-GACOS-CPS). The major difference between the SBAS-GACOS-CPS and SBAS-CPS is that the CPS method in SBAS-CPS estimates

443   the whole systematic and stochastic atmospheric delay on the assumption that they are

444   both randomly distributed in time. Whereas the CPS method in SBAS-GACOS-CPS

445   only estimates the residuals after GACOS corrections, which tends to better follow the

446   temporally random distribution because a large part of the atmospheric delays in each

447   interferogram has been corrected by GACOS.

448   Fig. 5 shows the example of InSAR cumulative displacements for the Sentinel-1

449   dataset on three acquisition dates in the summer of 2018 from the four abovementioned

450   methods. The uncorrected displacement maps (the first column) are contaminated by

451   significant stratified delays in the mountain regions in the northwest and southeast of

452   the basin. The effects of stratified delays were substantially mitigated by applying

453   GACOS correction for each interferogram, as shown in the second column. But

454   GACOS correction still left some residuals correlated with topography and short-

455   wavelength patterns in the results, especially on the acquisition 20180712. For

456   corrections only by applying the CPS method, however, significant residuals correlated

457   with elevation were found on all the three acquisitions (the third column). Similar

458   patterns in the residuals using CPS method were found on acquisitions in the summer

459   of 2017 and 2019, as shown in Supplementary Material (Figs. S2 and S3). This is

460   because the CPS method estimates the whole atmospheric delay by simply treating it

461   as random noise, whereas the atmospheric delay exists in seasonal and interannual

462   variations, i.e., it is temporally correlated, which leads to the residuals. For our

463   proposed method, the application of the GACOS correction can minimize the effect of

464   the temporally correlated parts of delays on each unwrapped interferogram and the

465   remaining errors were further reduced in the time series analysis by applying the CPS

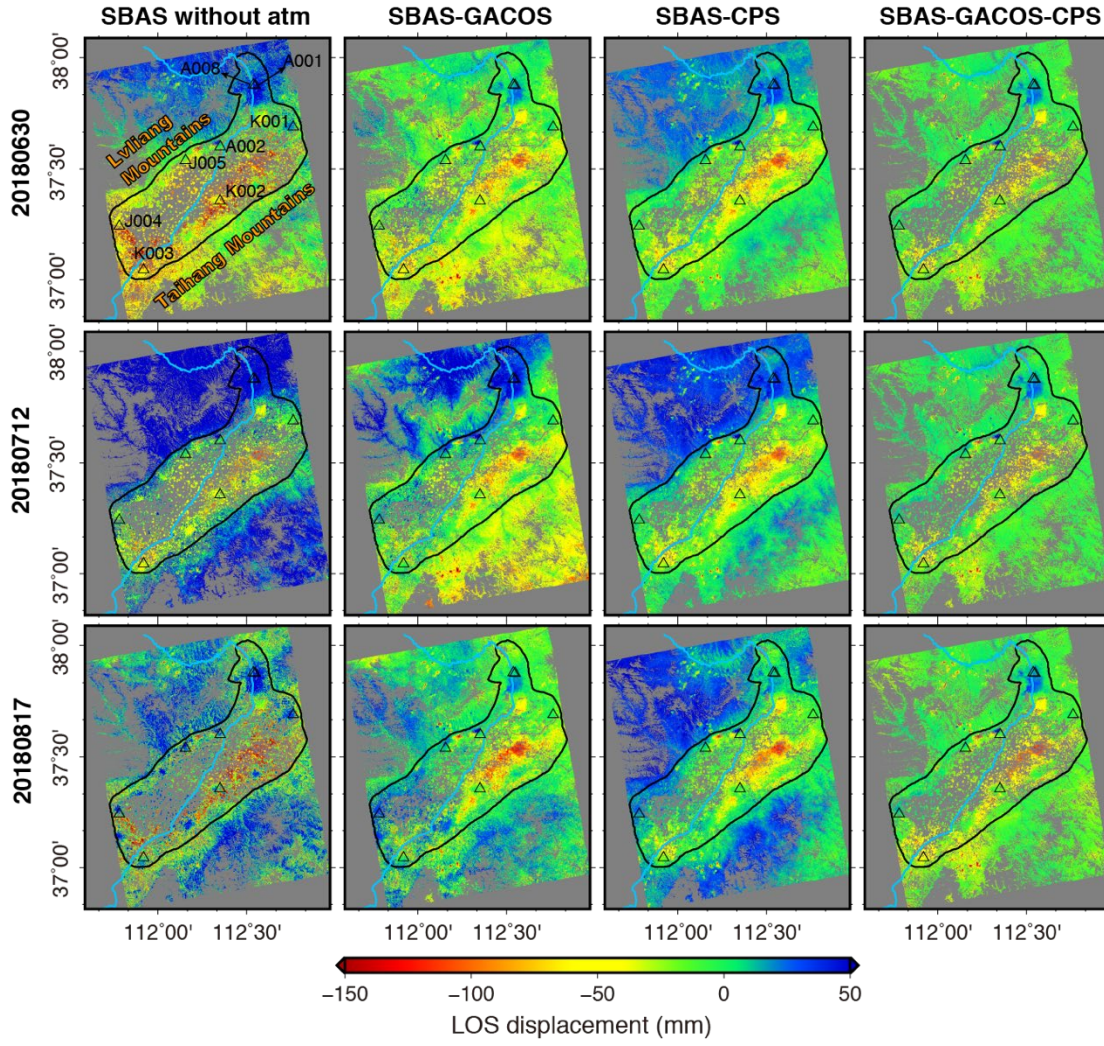466   method (second versus the fourth column in Fig. 5 as well as in Figs. S2 and S3).

Fig. 5. InSAR cumulative displacements with respect to the first acquisition (20170319) from Sentinel-1 on selected acquisition dates. The first row (left-to-right) represents displacement for acquisition date 20180630 from SBAS without atmospheric correction (SBAS without atm), with correction by GACOS (SBAS-GACOS), with correction by CPS (SBAS-CPS) and with correction by GACOS and CPS (SBAS-GACOS-CPS, our proposed approach), respectively. The second row and the third row are the same but for acquisition dates 20180712 and 20180817, respectively. The black triangles indicate the locations of CGPS sites. The displacements have spatially referenced to K001 site.

As discussed in Section 4.1, the GACOS fails to reproduce small-scale delay caused by the atmospheric turbulent process, as shown on the 20181028-20181109 interferogram in Fig. 4. The atmospheric turbulence occurred on 20181028 and

480 contaminated the displacement on this acquisition (Fig. 6a). One of the advantages of

481 our proposed method is that these small-scale and irregular features can be properly

482 estimated by the CPS method (Fig. 6b). After applying the correction, the displacement

483 map is considerably smoother (Fig. 6c). These results indicate that our proposed method

484 can mitigate the atmospheric delays more effectively and improve the accuracy of

485 ground displacement estimates.

486
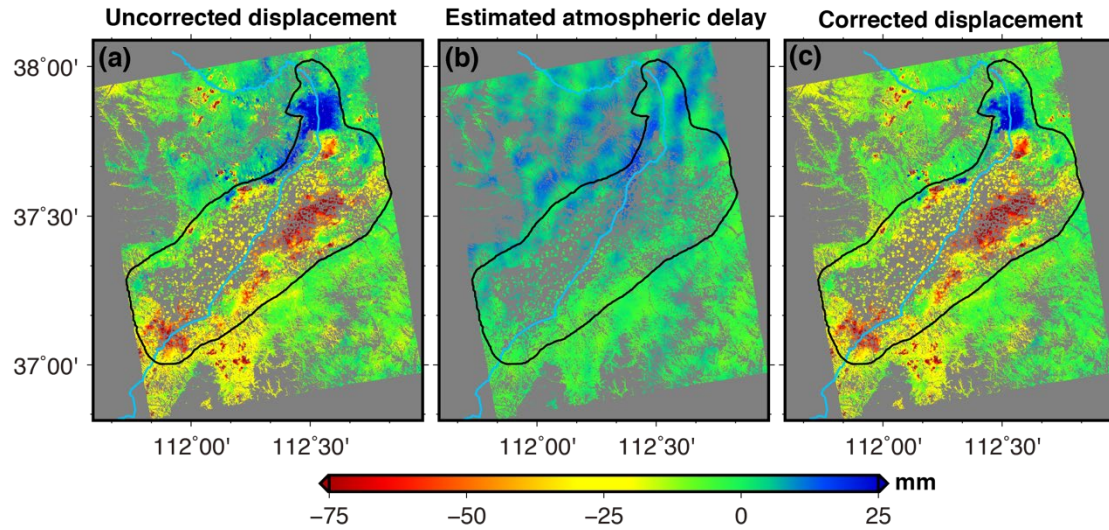
487 Fig. 6. (a) Uncorrected displacement on 20181028 with respect to the first acquisition

488 on 20170319. (b) Atmospheric delay estimated by the CPS method. (c) Displacement

489 after removing the estimated atmospheric delay.

490   Further validation was conducted by comparing InSAR displacements with

491 ground truth from CGPS stations, as shown in Fig. 7. From the uncorrected time series

492 (in blue), we obviously see the periodic oscillation with an annual cycle in the summer

493 between June and September, in which period the atmospheric water vapor is more

494 significant and more variable. Significant residuals remained in the time series using

495 GACOS correction (the purple color), while the corrected time series by CPS method

496 (the red color) are very clean and show good agreement with the CGPS measurements.

497 Although the time series corrected by CPS method (in green) also show considerable

498 reductions in the scatter, a bias between InSAR and CGPS measurements was found at

499 sites A001, A008 and K002. This can be observed on the acquisition 20180712 in Fig.

500 5, the uplift signals at sites A001 and A008 in Taiyuan city blurred in the result (the

third column) due to the remaining effects caused by the long-wavelength atmospheric delay, whereas the uplift signals are very clear in the SBAS-GACOS-CPS result (the fourth column). Because the CGPS sites A001 and A008 are only 800 meters apart, their displacement patterns are very similar. The RMSE between InSAR and GPS displacements improves from 19 mm without atmospheric corrections, to 11 mm by SBAS-CPS method, to 17 mm by SBAS-GACOS and to 8 mm by SBAS-GACOS-CPS method (our proposed approach), as shown in the Fig. 8.
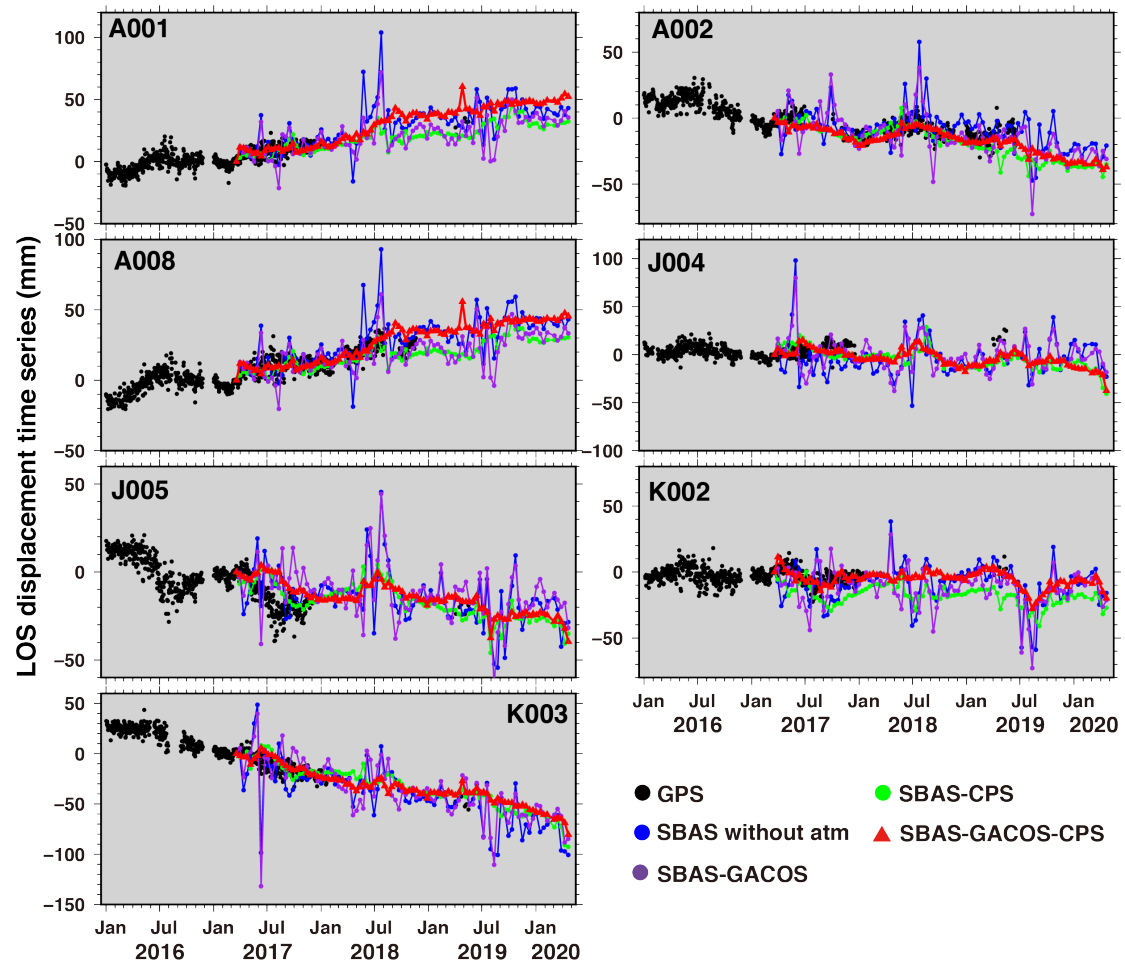
Fig. 7. Comparison of LOS displacement time series between InSAR and CGPS in the basin.
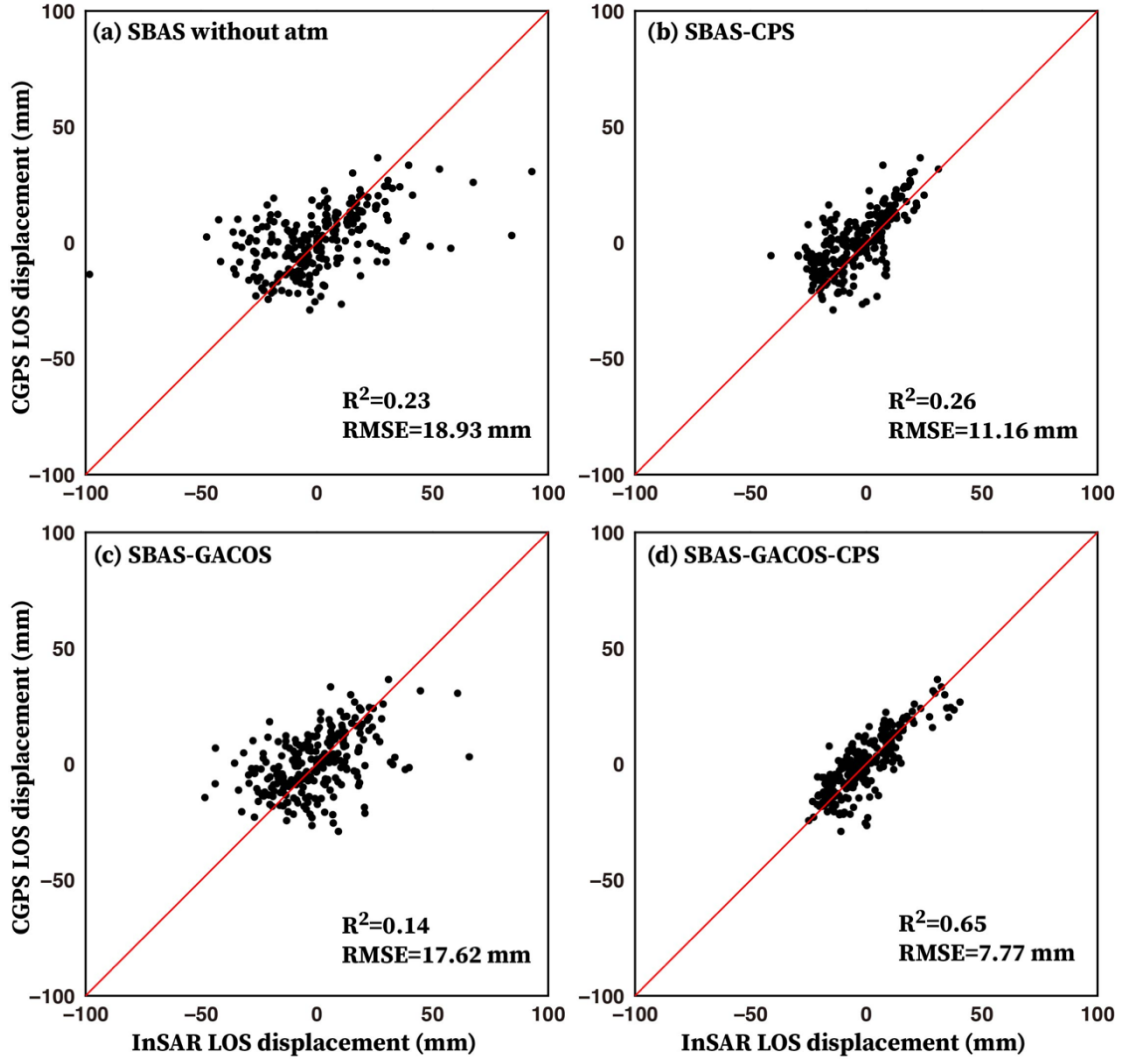
Fig. 8. Statistical comparison of cumulative displacements at overlapped acquisition times between InSAR and CGPS at all stations in Taiyuan basin. The R-square (R^2) and the Root Mean Squared Error (RMSE) are indicated in the figure.

5.2 InSAR deformation maps in Taiyuan basin

The InSAR ground deformation maps in LOS (line-of-sight) direction during different periods obtained from three SAR satellites are shown in Fig. 9. The subsidence areas spatially coincide with the groundwater drawdown cones (the dark red contours in Fig. 9), suggesting the excessive groundwater pumping is the driving factor of land subsidence. Comparing the velocity maps between the two observing periods 2007-2010 and 2017-2020, we found a general deceleration of land subsidence or even land uplift in the basin.

523   The LOS time series displacements at ten points (marked with black triangles and

524   labeled as TS-A to TS-J) located in the main deforming regions are shown in Figs. 10

525   and 11. Displacements at these points (except the points TS-D and TS-E) from ALOS-

526   1 (acquired in ascending orbit) and ENVISAT (acquired in descending orbit) show a

527   good agreement, suggesting that the displacements mostly occurred in vertical direction.

528   The reason of the discrepancy at points TS-D and TS-E is that the high displacement

529   rate (over 160 mm/yr at point TS-E) is detectable by ALOS-1 with longer radar

530   wavelength (L band, $\lambda = 23.6\ cm$) while it is aliasing in the short wavelength (C band,

531    $\lambda = 5.6\ cm$) of ENVISAT interferograms due to decorrelation effects (Lu et al., 2005).

532   These decorrelated effects can be observed in the interferograms shown in

533   Supplementary Material Fig. S4. The good agreement between results of ALOS-1 and

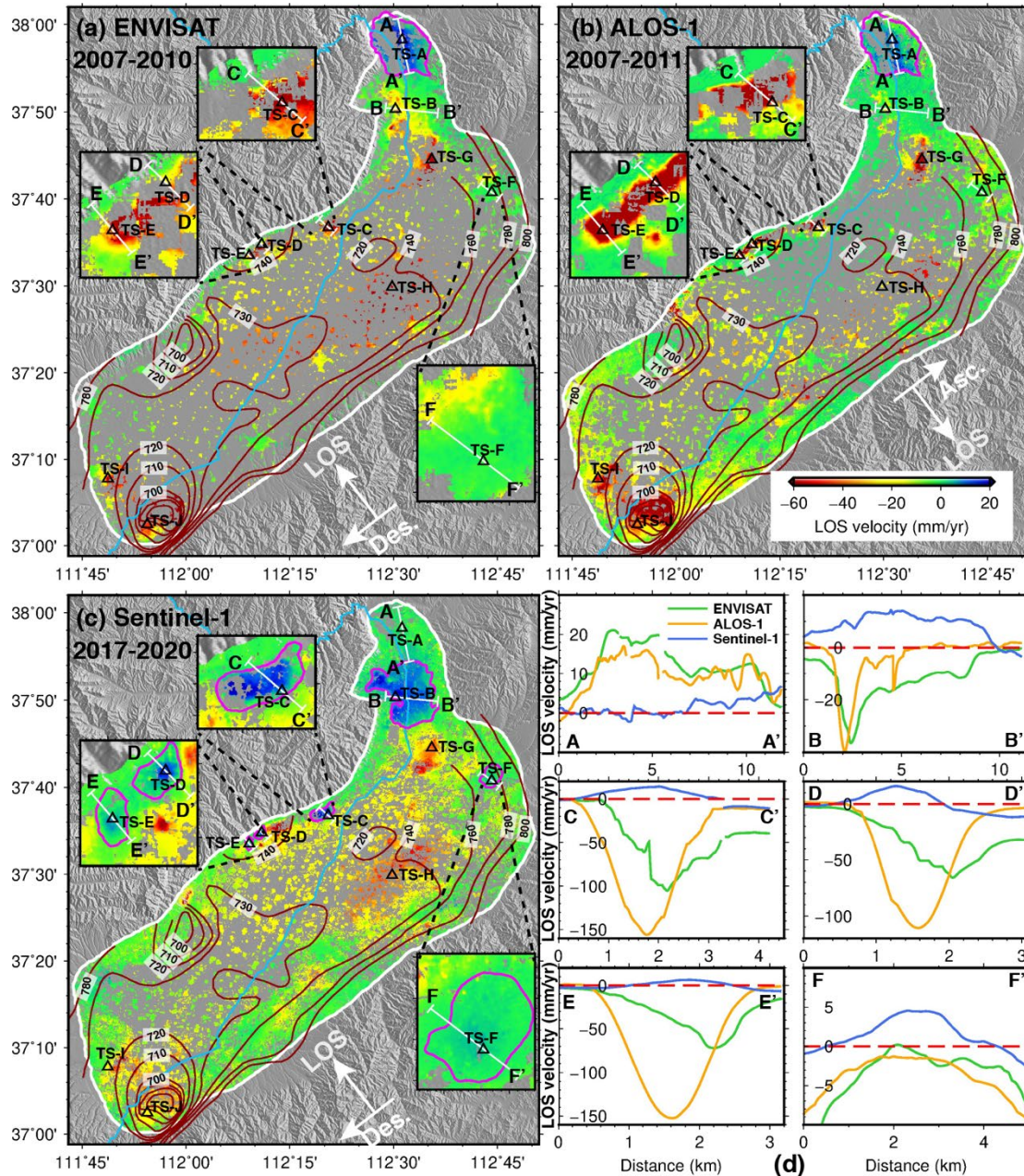534   ENVISAT also suggests our proposed InSAR analysis method is robust.

Fig. 9. InSAR average LOS deformation rates in Taiyuan basin: (a) January 2007-September 2010 from ENVISAT, (b) January 2007-March 2011 from ALOS-1 and (c) March 2017-April 2020 from Sentinel-1. The magenta polygons delineate the extents of the six uplifting areas in the basin. The black triangles show the locations of the displacement time series plotted in Figs. 10 and 11. (d) LOS velocities along profiles across the six areas experiencing land uplift. Contours in dark red represent groundwater level in 2011 (in meter) relative to sea level.

543   Land uplift were found in six areas (encircled with magenta polygons in Fig. 9).

544   Although large subsidence rates at profiles C-C', D-D' and E-E' were underestimated

545   by ENVISAT data, velocity profiles from different satellites during different time

546   periods show the spatial and temporal evolution of the deformation in these uplifting

547   areas (Fig. 9d). The north of Taiyuan city shows an uplifting rate of ~17 mm/yr at TS-

548   A during the period 2007-2010 while it tends to become stable during 2017-2020 with

549   a rate of only ~2 mm/yr (Fig. 10). This uplift pattern was also revealed by Liu et al.

550   (2018), where the authors measured an uplift rate larger than 10 mm/yr during 2004-

551   2005 in northern Taiyuan. The uplift region (see Fig. 9c) is located in the most densely

552   populated area in the city center of Taiyuan. This area suffered from the most severe

553   subsidence with a rate exceeding 110 mm/yr in 1980s measured from leveling (Ma et

554   al., 2005) and the rate decreased to ~40 mm/yr during 2007-2010 measured from InSAR

555   in this study. However, the land in this area reversed to uplift with a positive rate of

556   ~11 mm/yr at TS-B in the period 2017-2020. Three uplifting areas are located in the

557   western edge of the basin, where TS-C (Qingxu county), TS-D (between Qingxu and

558   Jiaocheng county) and TS-E (Jiaocheng county) resided. The most significant

559   subsidence occurred at TS-E with a rate up to ~163 mm/yr during 2007-2011 (ALOS-

560   1 result) and the land reversed to uplift during 2017-2020 with a rate of ~9 mm/yr. The

561   area located within the Jinzhong city where TS-F resided was subsiding with minor

562   rates between 5-10 mm/yr during 2007-2011 and was uplifting with rates of ~6 mm/yr

563   during 2017-2020. Land subsidence continues at points TS-G (south of Taiyuan city in

564   Xiaodian district), TS-H (west of Taigu county in the central basin), TS-I (south of the

565   basin in Xiaoyi city) and TS-J (south of the basin in Jiexiu city) (see Fig. 11), but the

566   rates significantly decreased, with rates reduction ranging from ~30% to ~70% between

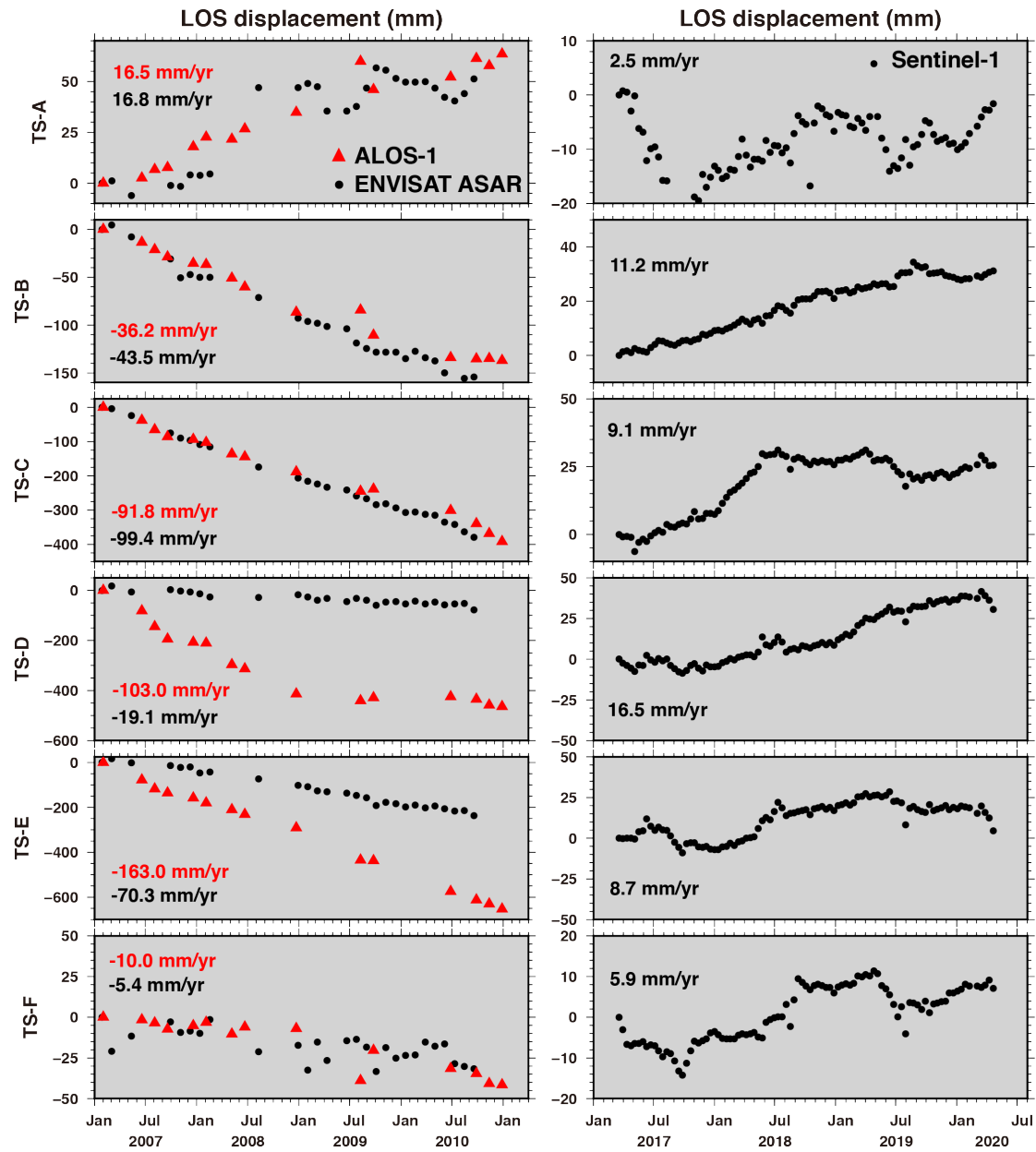567   the two time-spans (2007-2010 and 2017-2020).

Fig. 10. Displacement time series at points TS-A to TS-F. The ground at TS-A shows land uplift as detected by ENVISAT and ALOS-1 during 2007-2010 and stabilized during 2017-2020 as detected by Sentinel-1. The points TS-B to TS-F show land subsidence in the 2007-2010 period, while they reversed to land uplift in the 2017-2020 period.
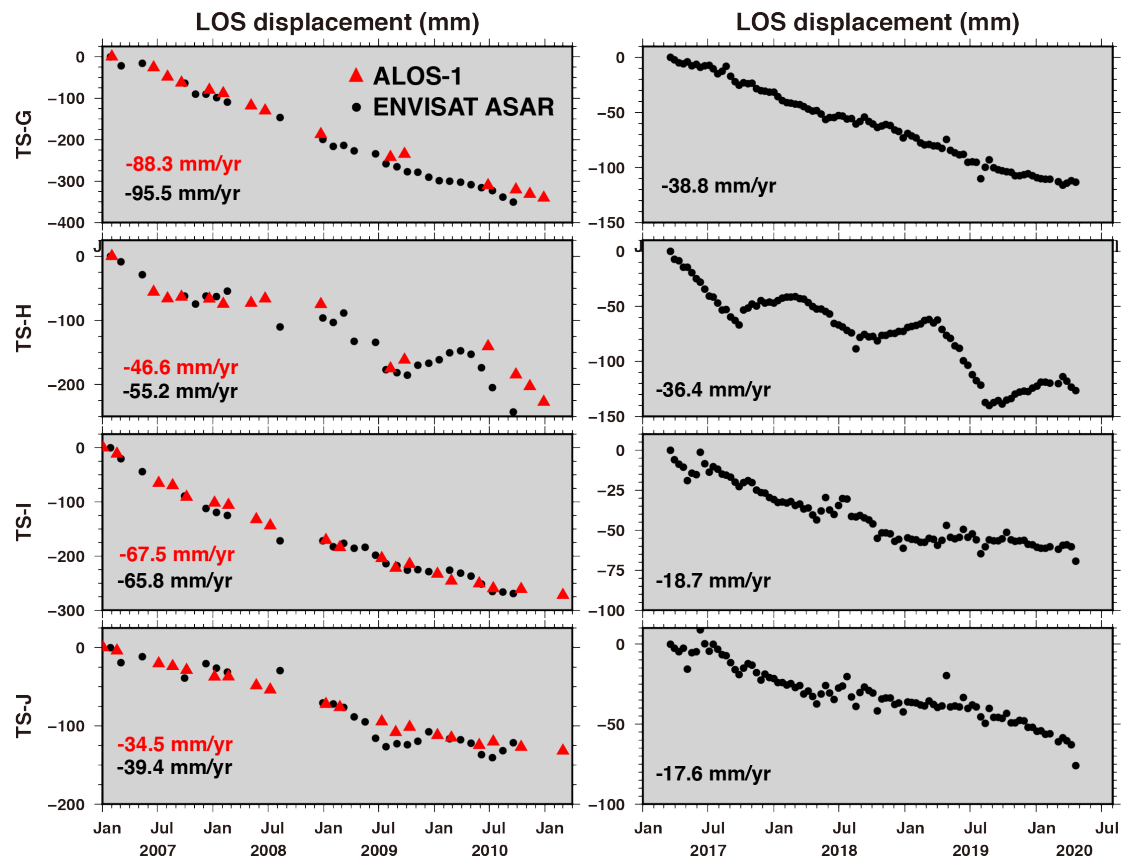
574

575 Fig. 11. Displacement time series at points TS-G to TS-J. Land subsidence is continuing

576 at these points but rates decrease.

577

578 **5.3 Seasonal amplitude and phase maps in the basin**

579   Annual or seasonal surface subsidence and uplift may present in response to

580 hydraulic head changes associated with natural or anthropogenic groundwater recharge

581 and discharge. The annual peak-to-peak amplitude and phase maps computed by

582 Equations (5) and (6) from InSAR displacement time series are shown in Fig.12. The

583 InSAR discrete coherent pixels were interpolated through the kriging geostatistical

584 method (Oliver and Webster, 1990) to obtain spatially continuous maps that are useful

585 for analyzing the spatial variability of the seasonal signals. We did not use ALOS-1

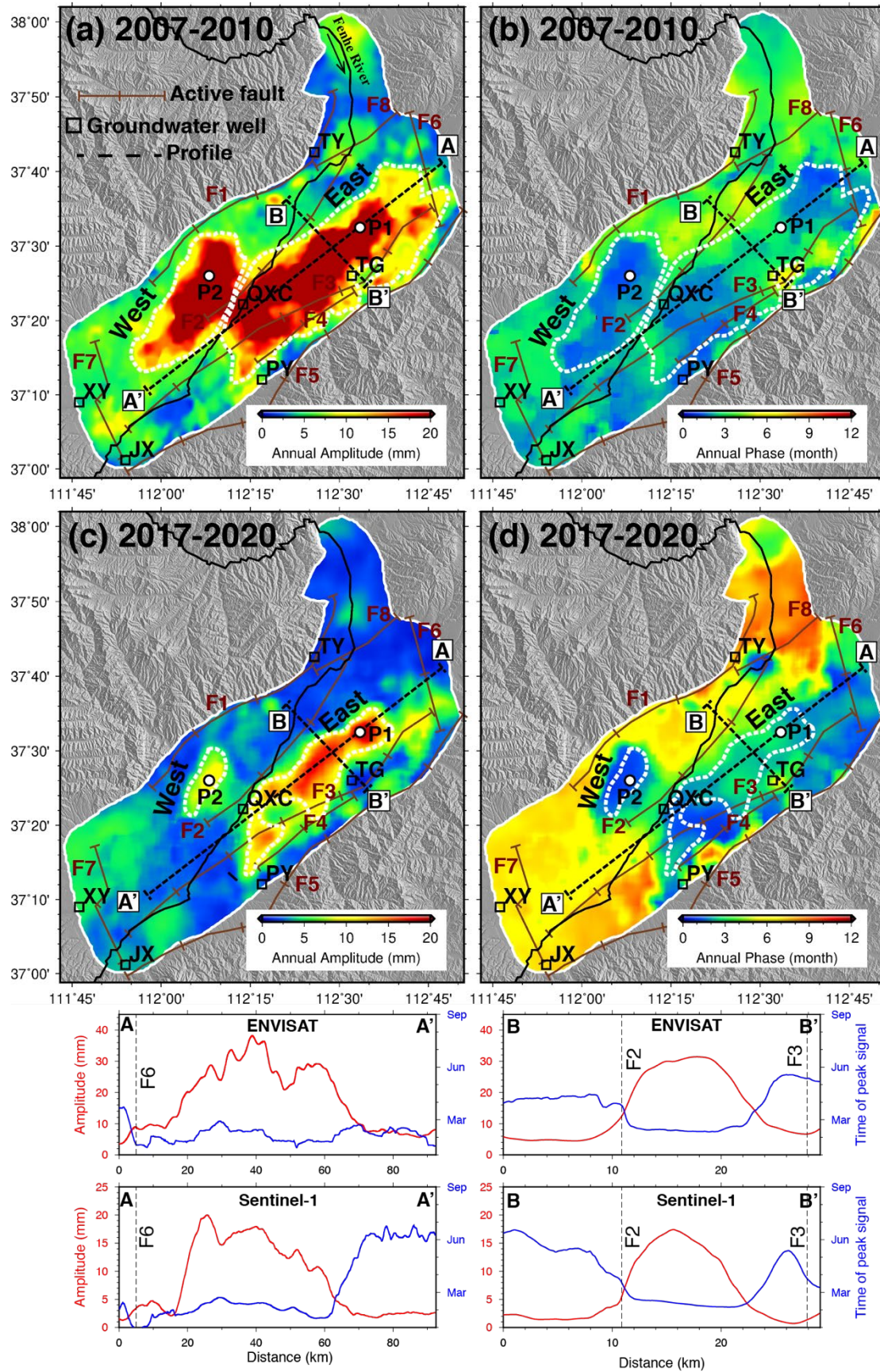586 results to model the seasonal signal because the data acquisitions are sparse in time.

29

587

Fig.12. Maps of annual peak-to-peak amplitude and phase delay. (a) and (b) are derived

from ENVISAT data, (c) and (d) are derived from Sentinel-1 data. The white dashed

polygons delineated the two sub-areas with significant annual amplitudes (> 10 mm), one in the west of the Fenhe River and the other in the east. The dashed black lines (A-A' and B-B') show the locations of the profiles used for the plots in the bottom. The white circle points (P1 and P2) show the location of the displacement time series in Fig.13. The black squares (TY, TG, QXC, PY, XY and JX) indicate the locations of the groundwater wells used for analysis in Section 6.1. The maps in the bottom are the annual peak-to-peak amplitude (red lines) and phase delay (blue lines) at profiles of A-A' and B-B'. F1-F8 indicate the active faults in the basin (refers to Fig. 2 for the fault names).

Most of the seasonal displacement is concentrated within the central basin corresponding to the main irrigated areas (Fig.12). In terms of the spatial distribution, there are two zones of peaks in the annual amplitudes in either side of the Fenhe River (encircled with the dashed white polygons with amplitudes > 10 mm in Fig.12). In general, we observed that the annual amplitude seems to be inversely correlated with the annual phase in the basin, i.e., higher amplitude regions peak earlier in the year, which implies that groundwater dynamics here follow a diffusion process (Riel et al., 2018). The discontinuity of both annual amplitude and phase maps in the east and west of the river, indicating the river plays some form of impediment on groundwater flow. The maximum peak-to-peak amplitude is 33 mm in the western zone and 43 mm in the eastern zone observed from ENVISAT data in the period of 2007-2010. These fluctuation magnitudes appear to decrease in the period 2017-2020, with the maximum amplitudes of only 10 mm and 20 mm in the western and eastern zone, respectively. This information indicates the changes of the pumping practices for the efforts to protect water resources in this vulnerable agricultural region.

The annual amplitudes change rapidly across faults (Fig.12). It can be found that the western zone is geologically bounded by the Jiaocheng fault (F1) in the west and Longjiaying fault (F2) in the east while the eastern zone is bounded by Longjiaying fault (F2) in the west and Qixian fault (F3) and Pingyao–Taigu fault (F4) in the east,

618 indicating that the fault is an effective barrier to across-fault fluid flow. This effect can

619 also be found in the maps of the annual phase where the ground in the west of the F2

620 fault has a peak signal in May-June whereas the ground in the east has a peak signal in
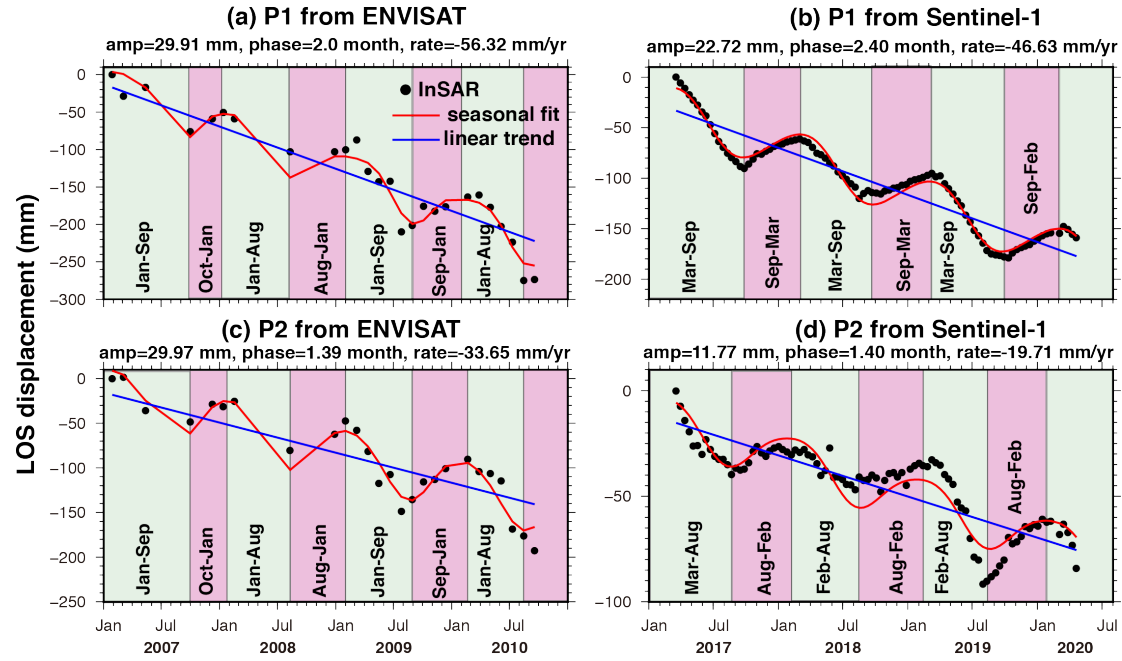
621 February-March (see B-B' profile in Fig.12).

Fig.13. InSAR LOS displacement time series at points P1 and P2 show a linear trend and seasonal fluctuation in the signal (see Fig.12 for point locations). The annual amplitude (amp), phase and rates are indicated in the figure.

We extracted displacement time series at two points P1 and P2 with the most significant seasonal signal located in the eastern and western zone (Fig.13), respectively. We can observe a clear seasonal elastic displacement embedded in the long-term trends of land subsidence at these two points. They have a negative peak (subsidence) in autumn (around August-September) and positive peak (uplift) in spring (around February-March). The time of peak signal at P1 is about one month earlier than that at P2, indicating the aquifer material in the location of P1 responses to groundwater recharge faster than the P2 location.

6. Discussion

6.1 Surface displacement response to groundwater level changes

The comparison of ground displacement time series with groundwater level changes at four wells in the basin are shown in Fig.14. Groundwater level rise occurred at well stations TY (+2.3 m/yr) and QXC (+0.6 m/yr) while water decline occurred at XY (-3 m/yr) and JX (-0.3 m/yr). With groundwater recovery, the land at TY reversed from subsidence (-1.5 mm/yr) in period 2007-2010 to land lift (+1.4 mm/yr) in period 2017-2020. However, regardless of the groundwater level rise at QXC, the land in this location continues to sink, but with the subsidence rate greatly reduced from -45.2 mm/yr in 2007-2010 to -23.1 mm/yr in 2017-2020. This continuing subsidence is likely caused by the residual compaction of slow draining aquitard layers due to the long-term decline of groundwater in the past decades, which might be at a scale of years to decades or more. Although a large groundwater drawdown rate of -3 m/yr was found at XY, the ground subsided at a much smaller rate (-6.7 mm/yr) in the period 2007-2010 and tend to be stable (only 0.8 mm/yr) in the period 2017-2020. At JX location, even though the water level declined with a small rate (-0.3 m/yr) during the period 2007-2020, the land subsidence rate was notably larger (-30.2 mm/yr) in the period 2007-2010 and reduced to -13.8 mm/yr in the period 2017-2020. The heterogeneity in the spatial distribution of aquifer and aquitard units contributes to the different responses of land deformation to groundwater level changes at these four water wells (Fig.14e). More detailed work needs to be done to understand the mechanics of aquifer systems and the spatial heterogeneity of aquifer system structure and material properties as well as for controlling groundwater pumping and land subsidence.
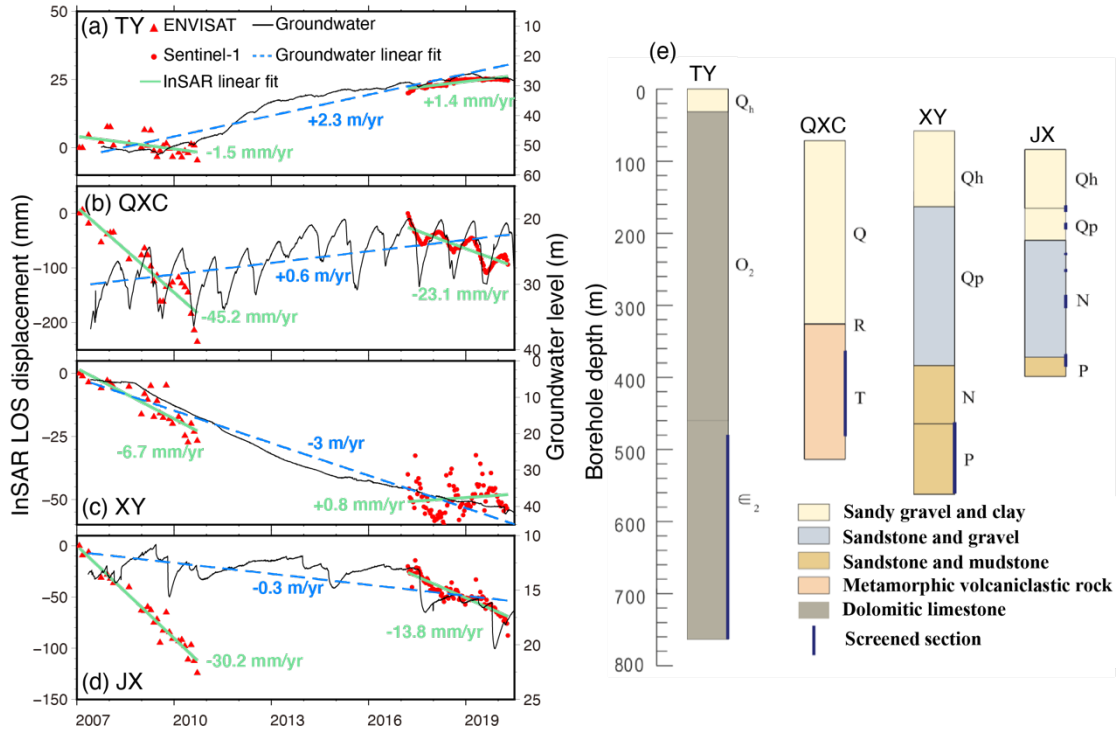
Fig.14. Comparison of InSAR LOS displacement time series and groundwater level changes at four water wells (a) TY, (b) QXC, (c) XY and (d) JX. Locations of water wells are found in Fig.12. The groundwater data is the value below ground surface level. (e) Aquifer geochronology and lithology in the four wells (Yan et al., 2020). The InSAR displacement between 2007 and 2010 are from ENVISAT while displacement between 2017 and 2020 are from Sentinel-1.

The causal relationships between ground displacement and water level were further quantitively analyzed at three water wells QXC, TG and PY, which are located in/near the area affected by large seasonal deformation (Fig.15). We find that negative peaks of land surface elevation and water levels reached in autumn (August-September) when the rainfall (gray stems in Fig.15) reached to the maximum. Corn crops are widely cultivated in this area (see Fig. 2b) and a large amount of water are demanded for irrigation. Generally, the pumping period is from March to August which causes the groundwater to drop sharply. The precipitation in the rainy season (June to September) reduces the pumping rates and the aquifer systems are naturally replenished. The groundwater starts to rise at the end of August and reaches back to the highest level in February-March since no agricultural irrigation in winter. This agricultural region was

selected as the pilot area with grant from Asian Development Bank (ADB) to support

676 climate change adaptation through groundwater management (Frank et al., 2016). With

677 this grant, farmers changed irrigation practices from flood to drip irrigation in their

678 greenhouses, leading to 40%–60% water savings. Simultaneously, the new systems

679 translated to 25%–40% crop yield increase. The upgrade in irrigation infrastructures

680 have been successful in halting the declining groundwater levels and mitigating further
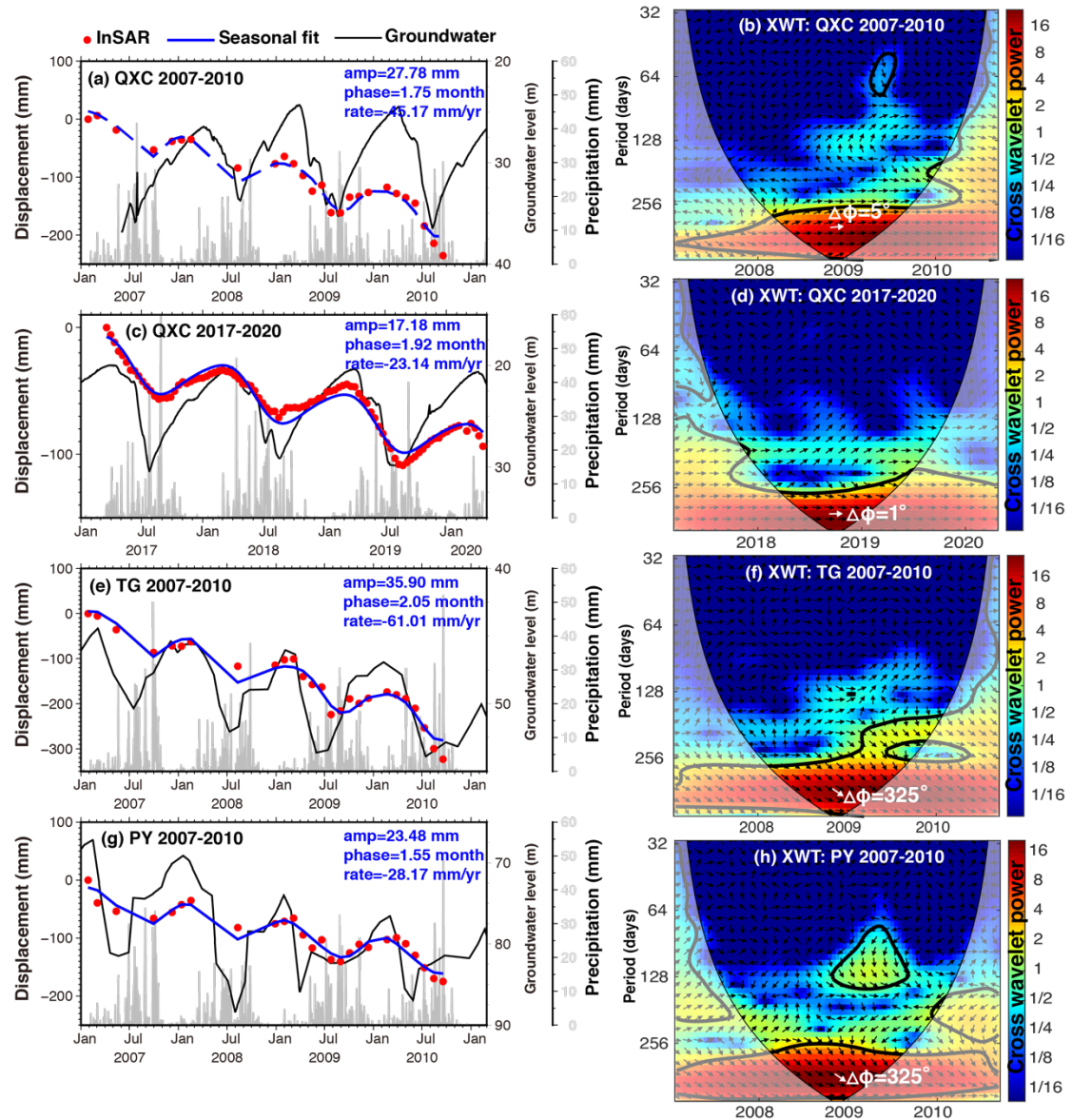
681 land subsidence in the central basin.

682

683 Fig.15. XWT cross-wavelet power spectra of ground displacement and groundwater

684 level time series at well locations QXC, TG and PY (see well location in Fig.12). The

685 color bar of XWT represents the common cross-wavelet power of both time series that

ranges from blue (low) to red (high). The arrows pointing right: in-phase correlations, left: anti-phase correlations. The 5% significance level against red noise is shown by the black contour. The lighter shade indicates the cone of influence (COI), where the analysis results are not reliable due to edge effects.

Regions with high cross-wavelet spectral power are evident at a period of 1 year for the three wells as observed in Figs. 15b, d, f and h. The phase shifts indicated in the figures are in correspondence to time lags of 5 days ($\Delta\emptyset = 5^{\circ}$) for QXC and 36 days ($\Delta\emptyset = 325^{\circ}$) for TG and PY, between land displacement and the forcing groundwater level changes. In heterogeneous aquifer systems, the delay between surface deformations caused by aquifer compaction and groundwater levels have been attributed to delayed fluid-pressure equilibration between the aquifers and aquitards (Hoffmann et al., 2003). In the aquifer system with sand and gravel layers, compaction reacts to water extraction almost instantaneously and can elastically rebound when water is recharged to the aquifer pore space. On the other hand, compaction of clay and silt rich layers (aquitards) is inelastic. In some systems with thick aquitards these delays can be on a time scale of years to decades or more (Bundschuh and Suarez Arriaga, 2010). Consequently, one month or less time delays between water levels and surface deformation at these three wells in the basin suggest that low-permeability clayey units in the region have a limited influence in delaying the compaction of the aquifer system. Such observations indicate that the aquifer maintains some capacity to recover storage capability. The cross-wavelet analysis therefore enables to track aquifer's health and highlight the system's sustainability in aiding the allocation of water resources for sustainable agricultural practices.

6.2 The effect of WWD project and restoration program on land subsidence in Taiyuan city

The evolution of groundwater level maps in Taiyuan city for the period of 1965–2019 are shown in Fig.16. Taiyuan city has been experiencing groundwater decline

713 since 1956. Before the 1980s, groundwater exploitation was in a state of anarchy. There

714 was no clear understanding of groundwater availability and no restriction to its usage.

715 At the time, though, the techniques of constructing water wells were not advanced;

716 hence, the amount of exploited groundwater was relatively modest and groundwater

717 table decline was small (Fig.16a). This situation changed sharply after 1980s, when a

718 large number of new wells were constructed with the rapid economic growth (Frank et

719 al., 2016). This extensive groundwater exploitation formed large regional cones of

720 depression (Figs.16b-i), inducing four land subsidence centers (Xizhang, Wanbailin,

721 Xiayuan and Wujiabao) by 2000 (Fig.16d). The subsidence began in the 1960s and

722 rapidly accelerated in 1980s-1990s because of the rapid increase in groundwater

723 exploitation, with accumulated subsidence exceeding 2.9 m by 2000 (Ma et al., 2006).

724 From 2001, the industrial development center moved to the suburb in the south of the

725 city (Tang et al., 2018), forming a new subsidence center in Xiaodian district (Fig.17a).

726 The land subsidence and uplift in Taiyuan city during a long time period from 1992 to

727 2015 have also been registered in Liu et al. (2018), which shows a similar pattern in

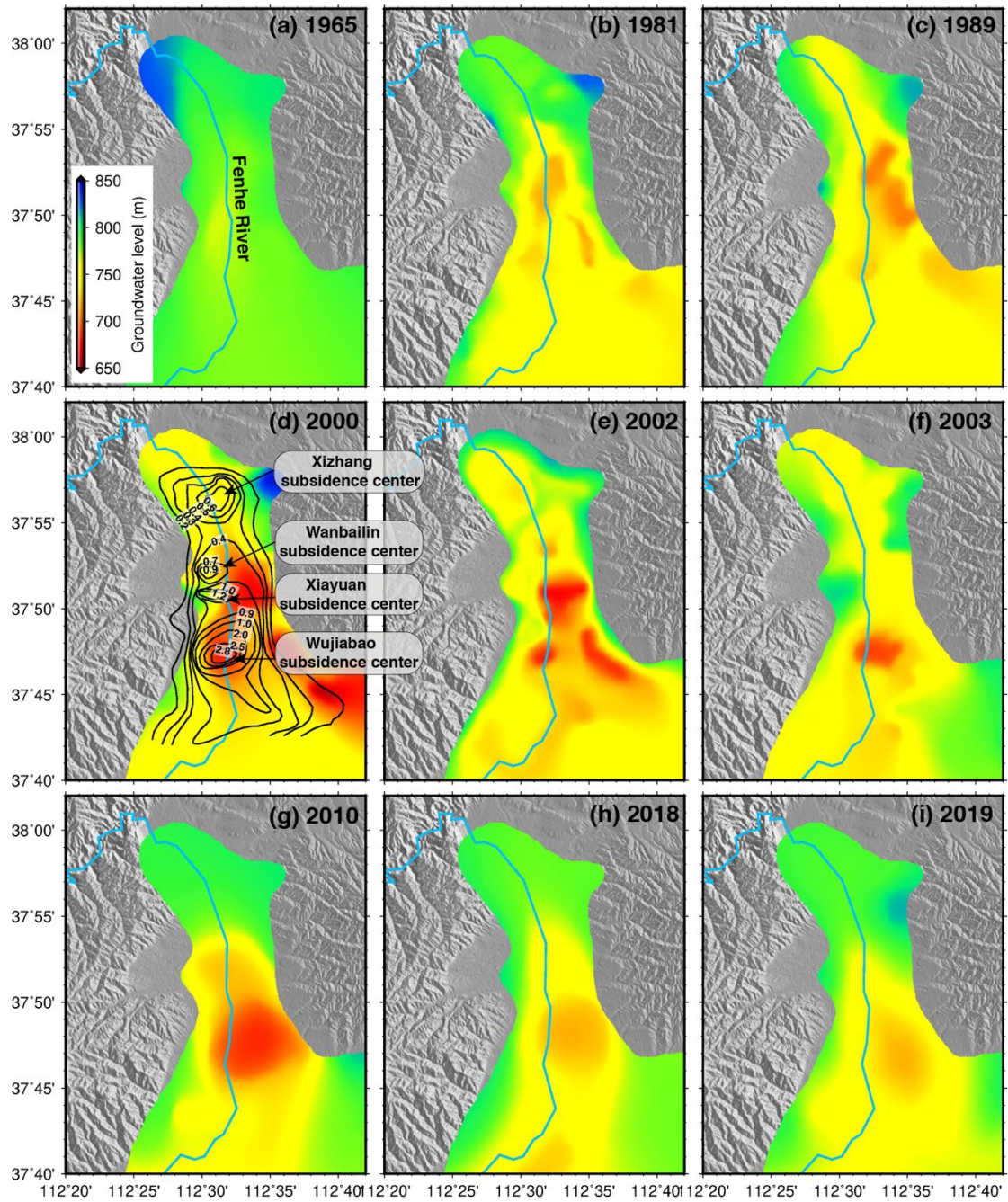728 spatial distribution of deformation with our results.

Fig.16. Groundwater level maps in Taiyuan city for the years: (a) 1965; (b) 1981; (c) 1989; (d) 2000; (e) 2002; (f) 2003; (g) 2010; (h) 2018; (i) 2019. Groundwater level data in (a), (b), (c) and (d) were collected from literature (Ma et al., 2006), (e) from (Ma et al., 2005), (f) from (Han et al., 2008), while (g), (h) and (i) were collected from Shanxi Provincial Department of Water Resources. The solid black lines in (d) are cumulative land subsidence contours for the period 1956-2000 (adapted from (Ma et al., 2006, 2005)). Four land subsidence centers (Xizhang, Wanbailin, Xiayuan and Wujiabao) were formed.

738   Since the operation of WWD project in 2003, the use of groundwater in Taiyuan

739   has been gradually replaced by water transferred from the Yellow River. As mentioned

740   earlier, the project has supplied 2.87 billion m^3 water (from 2003 to 2018) to Shanxi

741   Province, of which 1.219 billion m^3 to the city of Taiyuan, accounting for 65% of water

742   uses in this city. At the same time, the integrated restoration program (Fig.17f) actively

743   curtails extensive water use. The overexploited aquifer system has been receiving

744   natural recharge from precipitation and stream flow. As a result, groundwater level has

745   been gradually recovering, which is obviously recognizable on the water level maps

746   from 2002 to 2019 (Fig.16).

747   Groundwater level increments for the periods 2002-2010 (Fig.17c), 2002-2019

748   (Fig.17d), and 2010-2019 (Fig.17e) show that groundwater recovery was widespread

749   throughout the city. The increment maps for the periods 2002-2010 (Fig.17c) and 2002–

750   2019 (Fig.17d) demonstrate that the groundwater rebound evolved from the north to

751   the south, which is spatially consistent with efforts in groundwater management in

752   different stages (Fig.17f). The water table was first to rise from 2003 in the north

753   corresponding to the area of Fenhe River restoration phase I. After 2010, the rising of

754   groundwater levels in the north halted and the recovered water level are well

755   comparable with that from 1965 (Fig. 16a) when very few groundwater pumping was

756   carried out, indicating a complete aquifer recovery in this area. Water level increment

757   map for the 2010–2019 period (Fig.17e) suggests a reduction in the magnitude of

758   groundwater rise, with a maximum magnitude (approximately 50 m) occurred in the

759   central Taiyuan corresponding to the area of Fenhe River restoration phase II (Fig.17f).
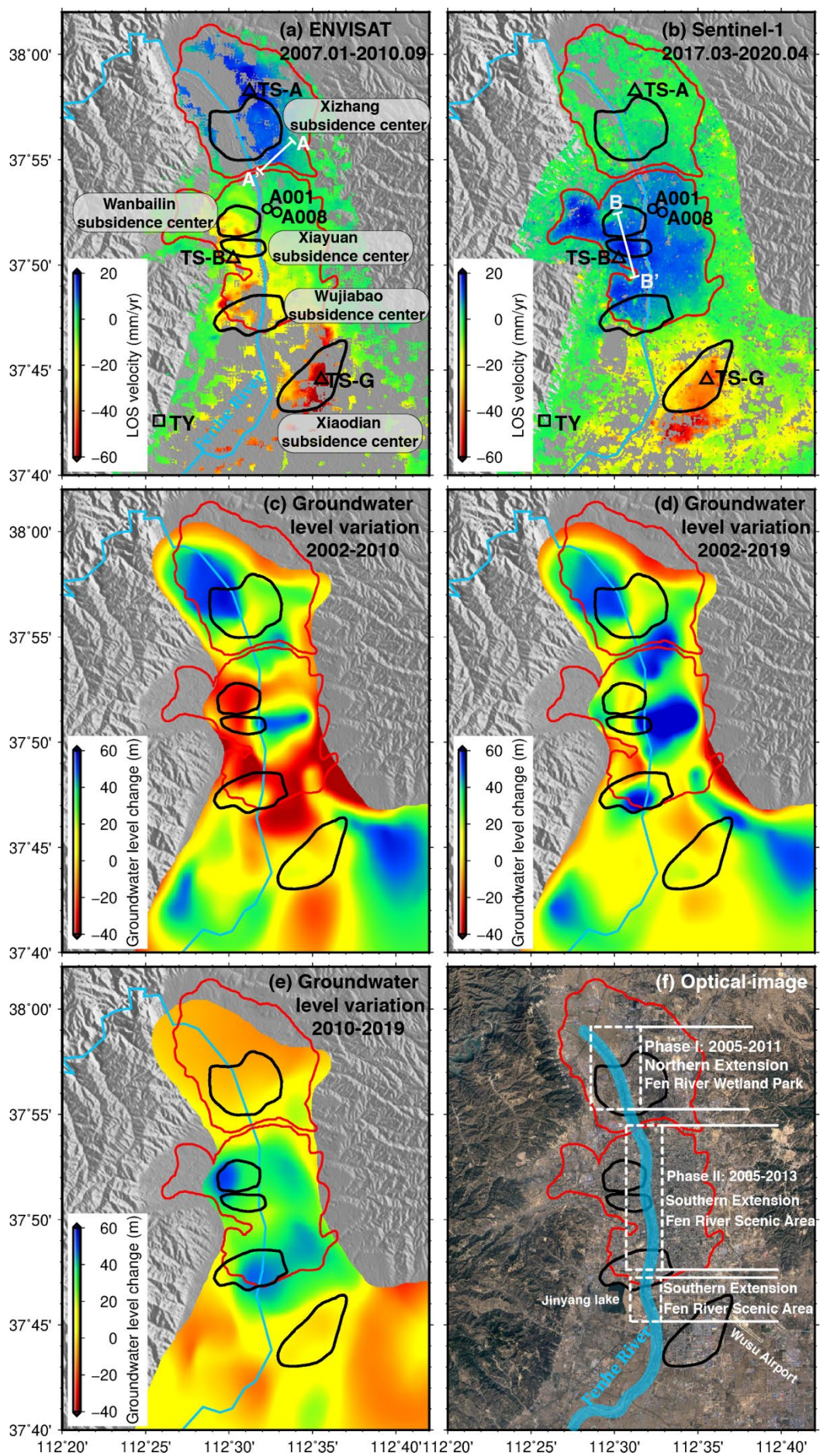
Fig.17. LOS displacement velocity maps in Taiyuan city in the periods (a) January 2007-September 2010 from ENVISAT and (b) March 2017-April 2020 from Sentinel-1. The red solid polygons denote the outlines of the uplifting areas. The black polygons indicate the old land subsidence centers. Groundwater level increments in the periods (c) 2002-2010, (d) 2002-2019 and (e) 2010-2019. (d) The optical image of Taiyuan shows the restoration efforts of waterfront redevelopment along the Fenhe River.

With groundwater recovery in the aquifer, land uplift was first found in the north (encircled with the north red polygon in Fig.17a) where it used to be a subsiding region (Xizhang subsidence center). The highest magnitude of water level rise in this area is ~60 m from 2002 to 2010 and the average land uplift rate is ~8 mm/yr in the period 2007-2010 observed from ENVISAT data. In the 2017-2020 period, the ground uplift in this area stopped (Fig.17b) due to the stabilization of groundwater table. The ground in the urban area in the old subsidence centers (Wanbolin, Xiayuan and Wujiabao) continued to sink in the ENVISAT period (Fig.17a), with a maximum subsiding rate of ~80 mm/yr in Wujiabao. In the Sentinel-1 period, the ground in these three subsidence centers reversed to uplift (encircled with the south red polygon in Fig.17b) with an average rate similar to the northern uplifting area (~8 mm/yr). The time series at point TS-B (Fig. 6) located in Xiayuan subsidence center clearly demonstrates this reversed displacement behavior between the two time periods. However, in the south (Xiaodian subsidence center), land subsidence is continuing in the period 2017-2020 with a rate of 38.8 mm/yr at TS-G, reducing ~50% relative to the period 2007-2010 (see time series at TS-G in Fig. 7). Although water transfer from the Yellow River eased the conflicting demand between municipal and industrial water supply in urban area (Yuan et al., 2018), more time is needed for sustainable groundwater recovery in the south of the city due to the intensive industrial water use in this region. However, the reduced rates of land subsidence provide an indication that water management practices are partly successful in mitigating further subsidence south of Taiyuan.
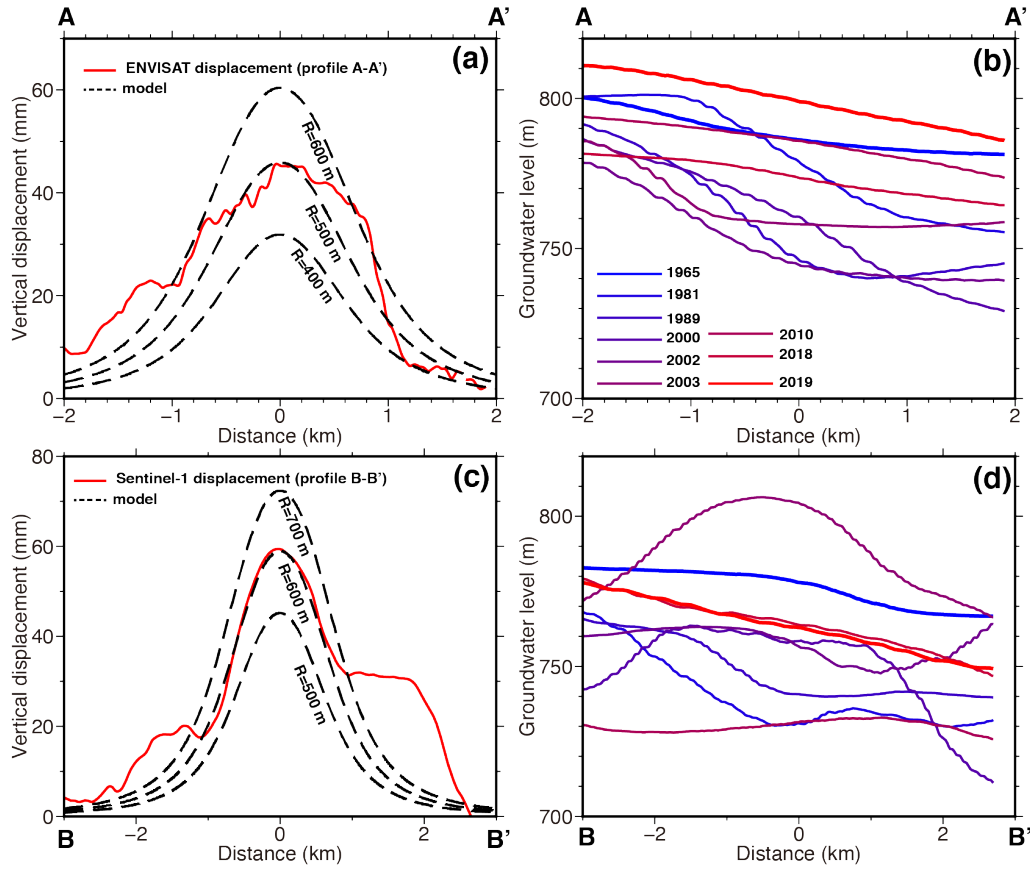
Fig.18. Comparison of InSAR observed uplift and theoretical displacement along (a) profile A-A' for assumed reservoir radius of 400, 500 and 600 m and along (c) B-B' for assumed reservoir radius of 500, 600 and 700 m. (b) and (d) are groundwater level changes along the two profiles obtained from groundwater level maps shown in Fig.16. For profile locations, refer to Fig.17.

The observed land uplift in Taiyuan can be attributed to pore pressure increase caused by rising groundwater (Terzaghi, 1925a). To describe this phenomenon, a simple analytical approach was applied to model surface displacement in an elastic medium due to the variation of pore pressure in an underlying reservoir (Geertsma, 1973). Groundwater level increased about 11 m along profile A-A' during the ENVISAT period and approximately 3.5 m along profile B-B' during the Sentinel-1 period. The resulting vertical surface deformation along these two profiles versus the radial coordinate are shown in Fig.18 and compared to the observed uplift from InSAR. As land subsidence and uplift mainly occur in vertical direction, we converted InSAR LOS (d_{los}) measurements into vertical dimension (d_v) using radar incidence angle θ,

804 $d_v = d_{los}/cos\theta$, with $\theta = 23°$ for ENVISAT and $\theta = 39.2°$ for Sentinel-1. As

805 shown in Fig.18, the theoretical displacements match the peak of the observed uplift

806 from InSAR, with assumed reservoir radius of 500 m at profile A-A' and 600 m at

807 profile B-B'. The shapes of the observed displacement at these two profiles are also

808 consistent with this simple model, although it is clear from Fig.18 that the underlying

809 reservoir is not simply circular. This first order model confirms that at least part of the

810 subsidence mechanism in Taiyuan city is elastically reversible rather than being totally

811 irreversible.

812 **6.3 InSAR as a supportive tool for groundwater management**

813   As a chronically dry region, hydraulic head data in Taiyuan basin was closely

814 monitored by well stations to track aquifer health in order to maintain sustainable

815 pumping practices. Measurements of surface displacement can complement hydraulic

816 head data for groundwater monitoring and management because surface displacement

817 reflect changes in groundwater storage below, which can be benefited from the high

818 resolution of InSAR technique.

819   In the case of short-period elastic aquifer displacement such as the observed

820 seasonal fluctuations in the central basin shown in Fig.15, the land subsidence and uplift

821 are directly correlated with groundwater level changes. As a consequence, the areas

822 with the highest levels of seasonal groundwater extraction directly correspond to the

823 areas with the highest amplitude of seasonal displacement. However, the seasonal land

824 subsidence and uplift were not proportional to the groundwater down and rise. For QXC

825 well location (Fig.15c), the water level dropped 9 m with a corresponding subsidence

826 of 63 mm between March to August in 2019. However, when the water level completely

827 recovered between August to March, the corresponding land uplift was only 33 mm.

828 The ratio of the change in displacement to the change in water level for the drawdown

829 portion (i.e., 7 mm/m) is twice larger than the ratio for the water level recovery portion

830 (3.7 mm/m), suggesting a large part of the displacement in the region is inelastic. The

831   concern here in this region is that it is located in an agricultural irrigated area with high

832   water stress and high groundwater demand, where groundwater pumping and aquifer

833   depletion is very common. Aquifer overexploitation could significantly impact food

834   production because ~60% of irrigation relies on groundwater (Frank et al., 2016).

835   Reducing demand for groundwater could mean reducing crop production, which will

836   pose threats to food security. Having a continuous map of displacement derived from

837   InSAR data allowed us to discover that there is about one-month delay between the

838   time when groundwater is pumped out of an aquifer and when the ground surface

839   deforms in response to the water withdrawal (Fig.15). These time-lag effects indicate

840   that, despite adverse impact of groundwater exploitation on irrigated aquifer, there are

841   opportunities for farmers to adapt to these seasonal changes and make a more

842   sustainable pumping scheme in such irrigated agriculture with declining aquifers.

843   Groundwater can be used more sustainably to maintain its buffer and contingency

844   supply to secure agricultural production in prolonged droughts when water demands

845   skyrocket.

846   In the case of delayed poroelastic rebound of aquitards, uplift can be time

847   dependent and gradually decrease after stabilization of the groundwater levels. The

848   curve of groundwater recovery and the surface uplift follow the shape of an exponential

849   function (Chaussard et al., 2016; Terzaghi, 1925b). This is the case for the uplift we

850   found in Taiyuan city. We performed the exponential regression at the TY well location

851   to both groundwater level and displacement by the form of $f(t) = \lambda(\exp(kt) - 1)$.

852    $f(t)$ is the groundwater level or deformation at time t, λ represents the coefficient

853   expressing the magnitude of uplift, and k is the decay coefficient describing the time

854   dependence of the uplift, which depends on the aquifer system properties

855   (compressibility and permeability) and ranges from -1 to 0 (the decay is fast when $k =$

856   -1, and displacement is close to linear when $k = 0$). The good fit between the

857   displacement and the exponential function (Fig.19b, red line, RMSE of 0.5) suggests

858   that the observed uplift can be explained by poroelastic rebound of the aquifer system

859 due to recovery of the water levels. This exponential relationship can be used to
860 describe the delayed response of fine-grained materials, which is described by the
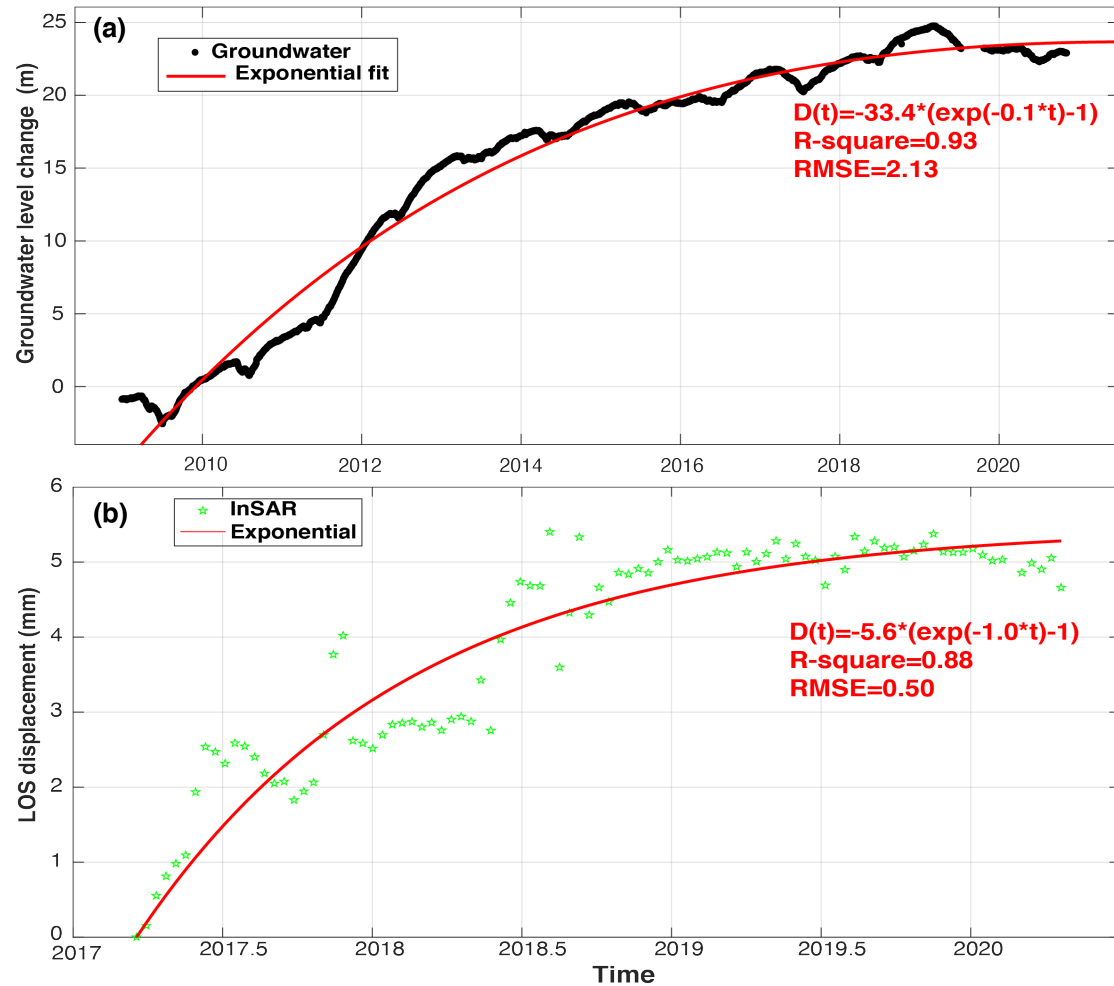861 theory of hydrodynamic consolidation (Terzaghi, 1925b).

862
863 Fig.19. (a) Groundwater level change at TY well between 2009 and 2020 and (b)
864 ground uplift at this location between 2017 and 2020 from Sentinel-1.

865 **7. Conclusion**

866   Taiyuan basin has been facing the problems of groundwater depletion and land
867 subsidence for a long time. The project of water transfer from Yellow River to Taiyuan
868 basin together with several restoration programs were designed to relieve water
869 shortage in the basin. In this paper, we have quantitatively evaluated the effects of these
870 measure in view of land subsidence hazards. In the context of the entire basin, the rising
871 groundwater level and in particularly the ground elevation rebound have been limited

in central and northern parts of the basin. In Taiyuan city, north of the basin, the rising groundwater level turned land subsidence with rates exceeding 110 mm/yr in the 1980 to land uplift with rates up to +25 mm/yr between 2017-2020. Rates in the other subsidence areas of the basin reduced by up to ~70% in the period 2017-2020 with respect to the period 2007-2010. Comparisons between trends of groundwater level and surface deformation suggest that the land uplift is linked to the poroelastic rebound mechanism in the aquifer system due to groundwater recovery.

By spatially interpolating the InSAR displacement data, a spatially continuous maps of annual amplitude and phase delay of ground displacement were obtained. In particular, we were able to detect the fine-scale features of seasonal displacement corresponding to one-year period (winter-summer cycles) typical of the expected variations in groundwater recharge and discharge due to agricultural irrigation in the central basin. The time lags between surface deformation and groundwater levels observed from cross-wavelet method are relatively short, which is one month or less, indicating that the low-permeability clayey units in the region have a limited influence in delaying the compaction of aquifer system. These fine-scale maps of seasonal deformation reveal the spatial variability of land surface in response to groundwater pumping and recharge. Our results show that analysis of InSAR time series data, particularly the data with improved temporal resolution and spatial coverage from Sentinel-1 mission, can be a useful tool for assessing the sustainability of groundwater pumping practices to aid water resources allocation in the background of large-scale water transfer project.

References

907 Bell, J.W., Amelung, F., Ferretti, A., Bianchi, M., Novali, F., 2008. Permanent
908   scatterer InSAR reveals seasonal and long-term aquifer-system response to
909   groundwater pumping and artificial recharge. Water Resour. Res. 44, n/a-n/a.
910   https://doi.org/10.1029/2007wr006152
911 Berardino, P., Fornaro, G., Lanari, R., Sansosti, E., 2002. A New Algorithm for
912   Surface Deformation Monitoring Based on Small Baseline Differential SAR
913   Interferograms. IEEE Trans. Geosci. Remote Sens. 40.
914   https://doi.org/10.1109/TGRS.2002.803792
915 Bundschuh, J., Suarez Arriaga, M.C., 2010. Introduction to the numerical modeling of
916   groundwater and geothermal systems: fundamentals of mass, energy and solute
917   transport in poroelastic rocks. CRC Press, Leiden, Netherlands.
918 Chaussard, E., Burgmann, R., Shirzaei, M., Fielding, E.J., Baker, B., 2016.
919   Predictability of hydraulic head changes and characterization of aquifer-system
920   and fault properties from InSAR-derived ground deformation. J. Geophys. Res.
921   Solid Earth 3782–3803. https://doi.org/10.1002/2015JB012608.Received
922 Chen, C.W., Zebker, H.A., 2001. Two-dimensional phase unwrapping with use of
923   statistical models for cost functions in nonlinear optimization. J. Opt. Soc. Am.
924   A 18, 338–351.
925 Chen, J., Ban, Y., Li, S., 2014. China: Open access to Earth land-cover map. Nature
926   514, 434–434. https://doi.org/10.1038/514434c
927 Chen, M., Tomás, R., Li, Z., Motagh, M., Li, T., Hu, L., Gong, H., Li, X., Yu, J.,
928   Gong, X., 2016. Imaging Land Subsidence Induced by Groundwater Extraction
929   in Beijing (China) Using Satellite Radar Interferometry. Remote Sens. 8, 468.
930   https://doi.org/10.3390/rs8060468
931 Chen, P., Wu, Q., Zhang, S., Wei, Y., 2003. Study of configuration of earth fissure in
932   Yuci. Northwest. Geol. 36.
933 Falke, M., 2016. The Fen River in Taiyuan, China: Ecology, Revitalization, and
934   Urban Culture. Environ. Soc. Portal, Arcadia. https://doi.org/10.5282/rcc/7679
935 Famiglietti, B.J.S., Ferguson, G., 2021. The hidden crisis beneath our feet.

936 Farr, T.G., Rosen, P.A., Caro, E., Crippen, R., Duren, R., Hensley, S., Kobrick, M.,
937   Paller, M., Rodriguez, E., Roth, L., Seal, D., Shaffer, S., Shimada, J., Umland, J.,
938   Werner, M., Oskin, M., Burbank, D., Alsdorf, D., 2007. The Shuttle Radar
939   Topography Mission. Rev. Geophys. 45, 1–33.
940   https://doi.org/10.1029/2005rg000183

941 Fattahi, H., Amelung, F., 2015. InSAR bias and uncertainty due to the systematic and
942   stochastic tropospheric delay. J. Geophys. Res. Solid Earth 120, 8758–8773.
943   https://doi.org/10.1002/2015JB012419

944 Feng, W., Zhong, M., Lemoine, J.M., Biancale, R., Hsu, H.T., Xia, J., 2013.
945   Evaluation of groundwater depletion in North China using the Gravity Recovery
946   and Climate Experiment (GRACE) data and ground-based measurements. Water
947   Resour. Res. 49, 2110–2118. https://doi.org/10.1002/wrcr.20192

948 Frank, S., Frank, R., Fan, G., Zhang, W., 2016. Agricultural production and
949   groundwater conservation: Examples of good practices in Shanxi province,
950   People's Republic of China. Mandaluyong City.

951 Fuhrmann, T., Garthwaite, M.C., 2019. Resolving three-dimensional surface motion
952   with InSAR: Constraints from multi-geometry data fusion. Remote Sens. 11.
953   https://doi.org/10.3390/rs11030241

954 Gee, D., Bateson, L., Grebby, S., Novellino, A., Sowter, A., Wyatt, L., Marsh, S.,
955   Morgenstern, R., Athab, A., 2020. Modelling groundwater rebound in recently
956   abandoned coalfields using DInSAR. Remote Sens. Environ. 249, 112021.
957   https://doi.org/10.1016/j.rse.2020.112021

958 Geertsma, J., 1973. Land subsidence above compacting oil and gas reservoirs. J. Pet.
959   Technol. 734–744.

960 Gong, H., Pan, Y., Zheng, L., Li, X., Zhu, L., Zhang, C., Huang, Z., Li, Z., Wang, H.,
961   Zhou, C., 2018. Long-term groundwater storage changes and land subsidence
962   development in the North China Plain (1971–2015). Hydrogeol. J. 26, 1417–
963   1427. https://doi.org/10.1007/s10040-018-1768-4

964 Grinsted, A., Moore, J.C., Jevrejeva, S., 2004. Application of the cross wavelet
965   transform and wavelet coherence to geophysical time series. Nonlinear Process.
966   Geophys. 11, 561–566. https://doi.org/10.5194/npg-11-561-2004

967 Guo, Q., Wang, Y., Gao, X., Ma, T., 2007. A new model (DRARCH) for assessing
968   groundwater vulnerability to arsenic contamination at basin scale: a case study in
969   Taiyuan basin, northern China. Environ. Geol. 52, 923–932.
970   https://doi.org/10.1007/s00254-006-0534-4

971 Haghshenas Haghighi, M., Motagh, M., 2019. Ground surface response to continuous
972   compaction of aquifer system in Tehran, Iran: Results from a long-term multi-
973   sensor InSAR analysis. Remote Sens. Environ. 221, 534–550.
974   https://doi.org/10.1016/j.rse.2018.11.003

975 Han, Y., Yan, S., Ma, H., Zhang, H., Wu, J., Wang, Y., Liang, X., Xu, H., Ma, T.,
976   Tang, Z., 2008. Investigation and Assessment of Groundwater Resources and
977   Their Environmental Problems in Six Basins of Shanxi Province. Geological

978   Publishing House, Beijing.

979   Herrera-García, G., Ezquerro, P., Tomás, R., Béjar-Pizarro, M., López-Vinielles, J.,
980   Rossi, M., Mateos, R.M., Carreón-Freyre, D., Lambert, J., Teatini, P., Cabral-
981   Cano, E., Erkens, G., Galloway, D., Hung, W.-C., Kakar, N., Sneed, M., Tosi,
982   L., Wang, H., Ye, S., 2021. Mapping the global threat of land subsidence.
983   Science (80-.). 371, 34 LP – 36. https://doi.org/10.1126/science.abb8549

984   Hoffmann, J., Galloway, D.L., Zebker, H.A., 2003. Inverse modeling of interbed
985   storage parameters using land subsidence observations, Antelope Valley,
986   California. Water Resour. Res. 39.
987   https://doi.org/https://doi.org/10.1029/2001WR001252

988   Hoffmann, J., Zebker, H.A., Galloway, D.L., Amelung, F., 2001. Seasonal subsidence
989   and rebound in Las Vegas Valley, Nevada, observed by synthetic aperture radar
990   interferometry. Water Resour. Res. 37, 1551–1566.
991   https://doi.org/10.1029/2000WR900404

992   Hooper, A., 2008. A multi-temporal InSAR method incorporating both persistent
993   scatterer and small baseline approaches. Geophys. Res. Lett. 35.

994   Jasechko, S., Perrone, D., 2021. Global groundwater wells at risk of running dry.

995   Kampes, B., Usai, S., 1999. Doris: the Delft Object-oriented Radar Interferometric
996   Software, in: 2nd International Symposium on Operationalization of Remote
997   Sensing. Enschede, The Netherlands.

998   Kinoshita, Y., Morishita, Y., Hirabayashi, Y., 2017. Detections and simulations of
999   tropospheric water vapor fluctuations due to trapped lee waves by ALOS-
1000   2/PALSAR-2 ScanSAR interferometry. Earth, Planets Sp. 69, 104.
1001   https://doi.org/10.1186/s40623-017-0690-7

1002   Liu, Y., Zhao, C., Zhang, Q., Yang, C., Zhang, J., 2018. Land Subsidence in Taiyuan,
1003   China, Monitored by InSAR Technique With Multisensor SAR Datasets From
1004   1992 to 2015. IEEE J. Sel. Top. Appl. Earth Obs. Remote Sens. 1–11.
1005   https://doi.org/10.1109/JSTARS.2018.2802702

1006   Long, D., Chen, X., Scanlon, B.R., Wada, Y., Hong, Y., Singh, V.P., Chen, Y., Wang,
1007   C., Han, Z., Yang, W., 2016. Have GRACE satellites overestimated groundwater
1008   depletion in the Northwest India Aquifer? Sci. Rep. 6, 1–11.
1009   https://doi.org/10.1038/srep24398

1010   Lu, Z., Wicks Jr., C., Kwoun, O., Power, J.A., Dzurisin, D., 2005. Surface
1011   deformation associated with the March 1996 earthquake swarm at Akutan Island,
1012   Alaska, revealed by C-band ERS and L-band JERS radar interferometry. Can. J.
1013   Remote Sens. 31, 7–20. https://doi.org/10.5589/m04-054

1014   Ma, R., Wang, Y., Ma, T., Sun, Z., Yan, S., 2006. The effect of stratigraphic
1015   heterogeneity on areal distribution of land subsidence at Taiyuan, northern
1016   China. Environ. Geol. 50, 551–568. https://doi.org/10.1007/s00254-006-0232-2

1017   Ma, T., Wang, Y., Yan, S., Ma, R., Yan, C., Zhou, X., 2005. Causes of Land
1018   Subsidence in Taiyuan City, Shanxi, China, in: Proceedings of the Seventh
1019   International Symposium on Land Subsidence. Shanghai, China, pp. 102–110.

Motagh, M., Shamshiri, R., Haghshenas Haghighi, M., Wetzel, H.-U., Akbari, B., Nahavandchi, H., Roessner, S., Arabi, S., 2017. Quantifying groundwater exploitation induced subsidence in the Rafsanjan plain, southeastern Iran, using InSAR time-series and in situ measurements. Eng. Geol. 218, 134–151. https://doi.org/10.1016/J.ENGGEO.2017.01.011

Motagh, M., Walter, T.R., Sharifi, M.A., Fielding, E., Schenk, A., Anderssohn, J., Zschau, J., 2008. Land subsidence in Iran caused by widespread water reservoir overexploitation. Geophys. Res. Lett. 35, L16403. https://doi.org/10.1029/2008GL033814

Oliver, M.., Webster, R., 1990. Kriging: a method of interpolation for geographical information systems. Int. J. Geogr. Inf. Syst. 4, 313–332. https://doi.org/10.1080/02693799008941549

Peng, J., Meng, L., Lu, Q., Deng, Y., Meng, Z., 2018. Development characteristics and mechanisms of the Taigu–Qixian earth fissure group in the Taiyuan basin, China. Environ. Earth Sci. 77, 1–20. https://doi.org/10.1007/s12665-018-7570-8

Pepe, A., Calò, F., 2017. A review of interferometric synthetic aperture RADAR (InSAR) multi-track approaches for the retrieval of Earth's Surface displacements. Appl. Sci. 7. https://doi.org/10.3390/app7121264

Qiao, X., Li, G., Li, M., Zhou, J., Du, J., Du, C., Sun, Z., 2011. Influence of coal mining on regional karst groundwater system: A case study in West Mountain area of Taiyuan City, northern China. Environ. Earth Sci. 64, 1525–1535. https://doi.org/10.1007/s12665-010-0586-3

Riel, B., Simons, M., Ponti, D., Agram, P., Jolivet, R., 2018. Quantifying Ground Deformation in the Los Angeles and Santa Ana Coastal Basins Due to Groundwater Withdrawal. Water Resour. Res. 54, 3557–3582. https://doi.org/10.1029/2017WR021978

Scanlon, B.R., Faunt, C.C., Longuevergne, L., Reedy, R.C., Alley, W.M., McGuire, V.L., McMahon, P.B., 2012. Groundwater depletion and sustainability of irrigation in the US High Plains and Central Valley. Proc. Natl. Acad. Sci. U. S. A. 109, 9320–9325. https://doi.org/10.1073/pnas.1200311109

Shamshiri, R., Motagh, M., Nahavandchi, H., Haghshenas Haghighi, M., Hoseini, M., 2020. Improving tropospheric corrections on large-scale Sentinel-1 interferograms using a machine learning approach for integration with GNSS-derived zenith total delay (ZTD). Remote Sens. Environ. 239, 111608. https://doi.org/10.1016/j.rse.2019.111608

Shanxi Provincial Bureau of Statistics, 2019. Shanxi Statistical Yearbook.

Shao, W., Cai, J., Liu, J., Luan, Q., Mao, X., Yang, G., Wang, J., Zhang, H., Zhang, J., 2017. Impact of water scarcity on the Fenhe river basin and mitigation strategies. Water 9. https://doi.org/10.3390/w9010030

Sun, X., Peng, J., Cui, X., Jiang, Z., 2016. Relationship between ground fissures, groundwater exploration and land subsidence in Taiyuan basin. Chinese J. Geol. Hazards Control 27, 91–98.

1062   Tang, Q., Xu, Q., Zhang, F., Huang, Y., Liu, J., Wang, X., Yang, Y., Liu, X., 2013.
1063   Geochemistry of iodine-rich groundwater in the Taiyuan Basin of central Shanxi
1064   Province, North China. J. Geochemical Explor. 135, 117–123.
1065   https://doi.org/10.1016/J.GEXPLO.2012.08.019
1066   Tang, W., Yuan, P., Liao, M., Balz, T., 2018. Investigation of Ground Deformation in
1067   Taiyuan Basin, China from 2003 to 2010, with Atmosphere-Corrected Time
1068   Series InSAR. Remote Sens. https://doi.org/10.3390/rs10001499
1069   Teatini, P., Gambolati, G., Ferronato, M., Settari, A. (Tony), Walters, D., 2011. Land
1070   uplift due to subsurface fluid injection. J. Geodyn. 51, 1–16.
1071   https://doi.org/https://doi.org/10.1016/j.jog.2010.06.001
1072   Terzaghi, K., 1925a. Principles of soil mechanics: IV. Settlement and consolidation of
1073   clay. Erdbaummechanic 95, 874–878.
1074   Terzaghi, K., 1925b. Principles of soil mechanics: IV. Settlement and consolidation of
1075   clay. Erdbaummechanic 95, 874–878.
1076   Thangarajan, M., Vijay P., S., 2016. Groundwater Assessment, Modeling, and
1077   Management, 1 st. ed. CRC Press, Boca Raton.
1078   Tomaoós, R., Pastor, J.L., Beoójar-Pizarro, M., Bonì, R., Ezquerro, P., Fernaoóndez-
1079   Merodo, J.A., Guardiola-Albert, C., Herrera, G., Meisina, C., Teatini, P., Zucca,
1080   F., Zoccarato, C., Franceschini, A., 2020. Wavelet analysis of land subsidence
1081   time-series: Madrid Tertiary aquifer case study, in: Proceedings of the
1082   International Association of Hydrological Sciences. pp. 353–359.
1083   https://doi.org/10.5194/piahs-382-353-2020
1084   Tong, X., Schmidt, D., 2016. Active movement of the Cascade landslide complex in
1085   Washington from a coherence-based InSAR time series method. Remote Sens.
1086   Environ. 186, 405–415. https://doi.org/10.1016/j.rse.2016.09.008
1087   Tymofyeyeva, E., Fialko, Y., 2015. Mitigation of atmospheric phase delays in InSAR
1088   data, with application to the eastern California shear zone. J. Geophys. Res. Solid
1089   Earth 120, 5952–5963. https://doi.org/10.1002/2015JB011886
1090   Waltham, T., 2002. Sinking cities. Geol. Today 18, 95–100.
1091   https://doi.org/10.1046/j.1365-2451.2002.00341.x
1092   Wang, K., Fialko, Y., 2017. Observations and Modeling of Coseismic and
1093   Postseismic Deformation Due To the 2015 M w 7 . 8 Gorkha (Nepal)
1094   Earthquake. https://doi.org/10.1002/2017JB014620
1095   Wessel, P., Luis, J., Uieda, L., Scharroo, R., Wobbe, F., Smith, W.H.F., Tian, D.,
1096   2019. The Generic Mapping Tools Version 6. Geochemistry, Geophys.
1097   Geosystems. https://doi.org/10.1029/2019GC008515
1098   Xie, Q., Guo, X., Ludwig, H.F., 1999. The Wanjiazhai Water Transfer Project, China:
1099   An environmentally integrated water transfer system. Environmentalist 19, 39–
1100   60. https://doi.org/10.1023/A:1006541023910
1101   Xie, X., Jiang, W., Sun, C., Yan, C., Feng, X., 2008. Comparison study on holocene
1102   paleoseismic activitiesamong multi-trenchesalong the Jiaocheng fault zone.
1103   Seism. Geol. 30.

1104   Xie, X., Jiang, W., Wang, H., Feng, X., 2004. Holocene activities of the Taigu fault
1105   zone, Shanxi province, in relation to the 1303 Hongdong M = 8 earthquake. Acta
1106   Seismol. Sin. 20.
1107   Xu, X., Sandwell, D.T., Tymofyeyeva, E., Gonzalez-Ortega, A., Tong, X., 2017.
1108   Tectonic and Anthropogenic Deformation at the Cerro Prieto Geothermal Step-
1109   Over Revealed by Sentinel-1A InSAR. IEEE Trans. Geosci. Remote Sens. 55,
1110   5284–5292. https://doi.org/10.1109/tgrs.2017.2704593
1111   Yan, R., Wang, G., Ma, Y., Shi, Z., Song, J., 2020. Local groundwater and tidal
1112   changes induced by large earthquakes in the Taiyuan Basin, North China from
1113   well monitoring. J. Hydrol. 582, 124479.
1114   https://doi.org/10.1016/j.jhydrol.2019.124479
1115   Yang, H., 2015. Simulation of Land Subsidence in Taiyuan basin. Chang'an
1116   University.
1117   Yu, C., Li, Z., Penna, N.T., 2018a. Interferometric synthetic aperture radar
1118   atmospheric correction using a GPS-based iterative tropospheric decomposition
1119   model. Remote Sens. Environ. 204, 109–121.
1120   https://doi.org/10.1016/j.rse.2017.10.038
1121   Yu, C., Li, Z., Penna, N.T., Crippa, P., 2018b. Generic atmospheric correction model
1122   for Interferometric Synthetic Aperture Radar observations. J. Geophys. Res.
1123   Solid Earth 1–21. https://doi.org/10.1029/2017JB015305
1124   Yuan, R., Zhang, W., Wang, P., Wang, S., 2018. Impacts of Water Transfer from the
1125   Yellow River on Water Environment in the Receiving Area of the Fenhe River.
1126   J. Nat. Resour. 33, 1416–1426. https://doi.org/10.31497/zrzyxb.20170691
1127   Zhao, Q., Ma, G., Wang, Q., Yang, T., Liu, M., Gao, W., Falabella, F., Mastro, P.,
1128   Pepe, A., 2019. Generation of long-term InSAR ground displacement time-series
1129   through a novel multi-sensor data merging technique: The case study of the
1130   Shanghai coastal area. ISPRS J. Photogramm. Remote Sens. 154, 10–27.
1131   https://doi.org/10.1016/j.isprsjprs.2019.05.005
1132
1133